ACS Catalysis

Research Article

Cite This: ACS Catal. 2019, 9, 7823–7839

pubs.acs.org/acscatalysis

Efficient Base-Metal NiMn/TiO_2 Catalyst for CO_2 Methanation

Wilbert L. Vrijburg,[†] Emanuele Moioli,[‡,§] Wei Chen,[†] Min Zhang,[†] Bas J. P. Terlingen,[†,∥] Bart Zijlstra,[†] Ivo A. W. Filot,[†] Andreas Züttel,[‡,§] Evgeny A. Pidko,[†,#] and Emiel J. M. Hensen*[,†]

[†]Laboratory of Inorganic Materials and Catalysis, Schuit Institute of Catalysis, Eindhoven University of Technology, P.O. Box 513, 5600 MB Eindhoven, The Netherlands

[‡]Laboratory of Materials for Renewable Energy (LMER), Institute of Chemical Sciences and Engineering (ISIC), Basic Science Faculty (SB), École Polytechnique Fédérale de Lausanne (EPFL), Valais/Wallis, Energypolis, 1951 Sion, Switzerland

[§]Empa Materials Science & Technology, 8600 Dübendorf, Switzerland

Supporting Information

ABSTRACT: Energy storage solutions are a vital component of the global transition toward renewable energy sources. The power-to-gas (PtG) concept, which stores surplus renewable energy in the form of methane, has therefore become increasingly relevant in recent years. At present, supported Ni nanoparticles are preferred as industrial catalysts for CO_2 methanation due to their low cost and high methane selectivity. However, commercial Ni catalysts are not active enough in CO_2 methanation to reach the high CO_2 conversion (>99%) required by the specifications for injection in the natural gas grid. Herein we demonstrate the promise of promotion of Ni by Mn, another low-cost base metal, for obtaining very active CO_2 methanation catalysts, with results comparable to more expensive precious metal-based catalysts. The origin of this improved performance is revealed by a combined approach of nanoscale characterization, mechanistic study, and density functional theory calculations. Nanoscale characterization with scanning transmission electron microscopy–energy-dispersive X-ray spectroscopy (STEM-EDX) and X-ray absorption spectroscopy shows that NiMn catalysts consist of metallic Ni particles decorated by oxidic Mn^{2+} species. A mechanistic study combining IR spectroscopy of surface adsorbates, transient kinetic analysis with isotopically labeled CO_2, density functional theory calculations, and microkinetics simulations ascertains that the MnO clusters enhance CO_2 adsorption and facilitate CO_2 activation. A macroscale perspective was achieved by simulating the Ni and NiMn catalytic activity in a Sabatier reactor, which revealed that NiMn catalysts have the potential to meet the demanding PtG catalyst performance requirements and can largely replace the need for expensive and scarce noble metal catalysts.

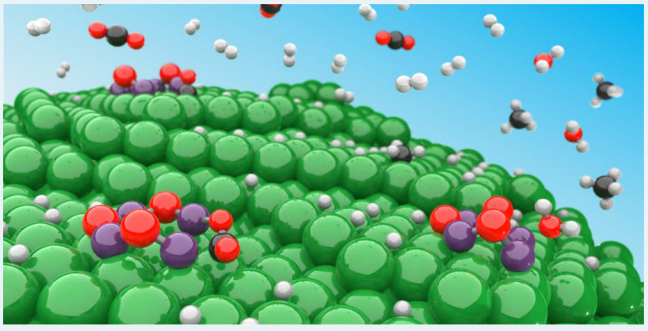

KEYWORDS: *CO_2 hydrogenation, nickel, manganese, synergy, mechanism*

1. INTRODUCTION

Concerns about the rising atmospheric levels of carbon dioxide (CO_2) are a major driver for the development of efficient and scalable technologies that can replace fossil energy resources. Abundant renewable energy sources such as solar photovoltaics and wind are expected to play a central role in this energy transition. Yet, the intermittent availability of wind and sunlight poses great challenges, when substantial amounts of fossil-based energy are to be replaced by renewable energy.[1,2] In order to balance supply and demand, there is an increasing need to store renewable electric energy. Among the many solutions, storage in chemical bonds brings advantages in terms of energy density, which is especially important with respect to seasonal storage, and compatibility with the current energy infrastructure. The hydrogenation of CO_2 to methane (CH_4) using hydrogen (H_2) obtained by water electrolysis constitutes a potentially scalable method to store renewable energy in a product with a high energy density, which can support the use of the existing infrastructure including transport over long distances and provide essential load balancing capacity. The synthesis of natural gas with H_2 originated from renewable resources is frequently discussed in the framework of the so-called power-to-gas (PtG) concept.[3−5] In addition to local energy storage, this concept reutilizes CO_2 either captured from the air, or available from other sources such as biogas. The first industrially developed hydrogenation reaction of CO_2 ("Sabatier" reaction) was based on a discovery made in 1902 by Sabatier and Senderens.[6] While superseded by the hydrogenation of carbon monoxide (CO, present in synthesis gas, which is a mixture of CO and H_2) derived from fossil feedstock for chemicals production (e.g., methanol) and later transportation fuels (Fischer–Tropsch synthesis), the Sabatier

Received: May 13, 2019
Revised: June 15, 2019
Published: July 17, 2019

reaction is currently receiving renewed interest in the context of renewable energy storage.[7−11] There are several recent reviews available on the Sabatier reaction.[12−17]

The Sabatier reaction requires active and selective catalysts to address the reactor design problem, i.e., to achieve a high conversion given the exothermic nature of the reaction.[10,18] Typical catalysts include supported metal nanoparticles such as Ru,[19−23] Rh,[24−26] and Pd.[27,28] Among these, Ru-based catalysts show the highest activity and CH_4 selectivity.[23] For CO methanation, which is an important step in commercial methane steam reformers to remove traces of CO (remaining after the water−gas shift reaction) during hydrogen production, Ni-based catalysts dispersed on oxide supports are preferred because of their considerably lower price in comparison to precious group metal catalysts.[12,29,30] Ni nanoparticle catalysts supported on Al_2O_3,[31−33] SiO_2,[34−36] and TiO_2[37,38] have been investigated for methanation processes. An issue in CO methanation is deactivation due to carbon deposition and Ni sintering.[16,39] These problems are usually less severe during the Sabatier reaction because of the lower CO pressure, which leads to a lower rate of carbon deposition and a lower likelihood of $Ni(CO)_4$ formation. Concerning the mechanism of CO_2 methanation, one can distinguish pathways in which CO_2 is transformed into CO either directly,[36,40,41] via a formate intermediate,[42−45] or via oxygenate intermediates.[46,47] The exact mechanism will depend on the metal and possible promoters.[39] The further conversion of CO to CH_4 follows most likely classical pathways involving surface CH_x intermediates.[48]

Practical CO_2 methanation for energy storage will require compact single-unit catalytic reactors for small-scale operation in which the reaction must be self-sufficient for off-grid operation. A recent study by Moioli et al. demonstrated that Ru catalysts allow operating a catalytic Sabatier reactor in autothermal mode reaching CO_2 conversions higher than 99.5% required for PtG energy storage.[49] Although Ru has the intrinsic activity to achieve high conversion, it is considered too costly for large-scale energy storage.[12] Accordingly, it is desirable to develop more active Ni catalysts for the Sabatier reaction. Among bimetallic catalysts based on combinations of Ni and other base metals, Fe and Co have also been explored as promoters for CO_2 methanation catalysts with benefits in terms of the CH_4 yield.[50,51] A promoter element for Ni that has received relatively little attention in this context is Mn. This is surprising as NiMn catalysts were already investigated as potential Fischer−Tropsch catalysts as early as the 1920s.[52] CoMn catalysts are active Fischer−Tropsch catalysts, and the subject of several investigations in the past decade.[53−56] In recent reports, the addition of Mn to Ni/Al_2O_3 has been explored for CO and CO_2 methanation, the synergy being attributed to a higher Ni dispersion.[57−59] The group of Stockenhuber studied the influence of a range of transition metals including Mn on Ni/Al_2O_3 catalysts on CO activation.[60] In addition, Burger et al. prepared catalysts via coprecipitation and determined that adding manganese to Ni/Al_2O_3 increased the CO_2 adsorption capacity of the catalyst which was used to explain the higher methanation rate.[61] Despite these initial works, a detailed understanding of the nature and potential of bimetallic NiMn methanation catalysts and the role of the Mn promoter is still limited.

In the present study we report a strong promotional effect of Mn on Ni/TiO_2 catalysts for CO_2 and CO methanation, explain the nanoscale origins of the Ni−Mn synergy, and demonstrate its potential in replacing Ru in self-sustained Sabatier reactors relevant for application in PtG processes. At the nanoscale, we investigate the origin of this synergy using electron microscopy and X-ray absorption and IR spectroscopy supplemented by a first-principles density functional theory study of the mechanism of the Sabatier reaction of Ni and NiMn based catalysts. Experimental catalytic activity data supported by transient isotopic kinetic data are related to predictions by microkinetics simulations based on reaction energy diagrams. At the reactor scale, we demonstrate the promise of an optimized NiMn catalyst by showing that this combination can obtain almost the same performance as an Ru-based catalytic bed in a Sabatier reactor.

2. METHODS

2.1. Catalyst Preparation. The titania support used in this study was AEROXIDE TiO_2 P-25 (Evonik), which is a fine-particulate, pure titanium dioxide with a high specific surface area (BET surface area 50 m^2/g) containing both rutile and anatase crystal structures. $Ni(NO_3)_2{\cdot}6H_2O$ (99.9%) and $Mn(CH_3COO)_2{\cdot}4H_2O$ (99.9%) were obtained from Sigma-Aldrich and were used without further purification. In a typical procedure, $Ni(NO_3)_2{\cdot}6H_2O$ (0.297 g) and $Mn(CH_3COO)_2{\cdot}4H_2O$ (0−0.501 g) were dissolved in 6 mL deionized H_2O. An appropriate amount of TiO_2 (ca. 2 g) was slowly added to the aqueous solution under stirring at room temperature. This suspension was left for 3 h and then heated to 80 °C to remove excess H_2O. The obtained solid was finally dried overnight at 110 °C in a static air oven.

2.2. Characterization. *2.2.1. Elemental Analysis.* The metal content of the samples was determined by ICP-OES using a Spectro Blue ICP apparatus. Samples were dissolved in a concentrated solution of 2 mL HNO_3 and 5 mL H_2SO_4 at 250 °C.

2.2.2. X-ray Diffraction (XRD). Crystalline phases in the samples were investigated using XRD. Powder XRD patterns were recorded on a Bruker D2 Phaser diffractometer using Cu Kα radiation with a wavelength of 1.54 Å. The 2θ angle was varied between 10 and 80° with a step size of 0.02° at 1.0 s/step.

2.2.3. CO Chemisorption. The available metal sites were probed by CO chemisorption using a Micromeritics ASAP 2020. Typically, 100 mg catalyst was loaded into a quartz U-tube reactor. Prior to CO chemisorption, the sample was reduced at 450 °C after heating to this temperature at a rate of 5 °C/min and followed by an isothermal dwell of 4 h. After evacuation at 470 °C to remove all hydrogen species, CO chemisorption was carried out at 35 °C.

2.2.4. Temperature-Programmed Reduction (TPR). The reduction of the samples was investigated using H_2-TPR. Measurements were performed using a Micromeritics Autochem II 2920 equipped with a fixed-bed U-tube reactor, a furnace, and a thermal conductivity detector. Typically, 100 mg catalyst was loaded in a quartz reactor. H_2-TPR was carried out in 4% H_2 in N_2 at 50 mL/min between 50 and 900 °C at 10 °C/min. The H_2 signal was calibrated using a CuO/SiO_2 reference catalyst.

2.2.5. Quick X-ray Absorption Fine Structure (QEXAFS). The oxidation state and structure of the Ni and Mn phases were studied during catalyst reduction using QEXAFS. Measurements were done at the Ni K-edge (8.3 keV) and the Mn K-edge (6.5 keV) in transmission mode on beamline B18 at Diamond Light Source (Didcot, United Kingdom). The

DOI: 10.1021/acscatal.9b01968
ACS Catal. 2019, 9, 7823−7839

energy was selected with a Si(111) monochromator. Energy calibration was done using Ni (E_0 = 8.333 keV) and Fe (E_0 = 7.112 keV) foils for Ni and Mn K-edge measurements, respectively. The photon flux of the incoming and outgoing X-ray beam was detected with two ionization chambers I_0 and I_t, respectively. The obtained absorption data were background subtracted, normalized, and fitted as difference spectra using Athena software. EXAFS analysis was performed using Artemis on k^3-weighted data. The amplitude reduction factor S_0^2 was determined by fitting the first and second shell Ni−O and Ni−Ni coordinations to 6 and 6, respectively, of a β-Ni(OH)$_2$ reference sample measured at the Ni K-edge (8.3 keV).

In a typical experiment, ca. 50 mg catalyst sample was placed in a stainless-steel XAS reactor equipped with two fire-rods and diamond or glassy carbon windows as described elsewhere.[62] Catalysts were reduced in this cell by heating at a rate of 5 °C/min to 450 °C followed by an isothermal dwell of 2 h in a flow of 10 vol % H_2 in He at a total flow rate of 25 mL/min. After this reduction treatment, the temperature was lowered to room temperature. Reduced catalysts were exposed to a CO_2/H_2/He gas mixture with a volumetric composition of 2/8/90 at a total flow rate of 25 mL/min. The catalyst sample was heated to 350 °C at a rate of 5 °C/min followed by an isothermal dwell of 2 h. After this procedure, the temperature was again lowered to room temperature. Selected catalysts were exposed to a CO/H_2/He gas mixture with a volumetric composition 2/6/92 at a total flow rate of 25 mL/min ration. The catalyst was subjected to the same temperature program as during the CO_2 hydrogenation measurements. During the reaction experiments, the state of the samples was followed by XANES, while EXAFS spectra were recorded at room temperature before and after the reactions.

2.2.6. STEM-EDX. The average particle size, the particle size distribution, and the nanoscale distribution of elements in the samples was studied using scanning transmission electron microscopy−energy-dispersive X-ray spectroscopy (STEM-EDX). Measurements were carried out on a FEI cubed Cs-corrected Titan operating at 300 kV. Samples were crushed, sonicated in ethanol, and dispersed on a holey Cu support grid. Elemental analysis was done with an Oxford Instruments EDX detector X-Max^N 100TLE. Due to carbon contamination during acquisition of elemental maps, each area was only measured once.

2.2.7. Temperature-Programmed Hydrogenation (TPH). The coke content of the catalysts was determined by removing the coke as methane using TPH. Typically, 50 mg catalyst and 150 mg SiC were loaded in a quartz reactor. Samples were reduced by heating to 450 °C at a rate of 5 °C/min followed by an isothermal dwell of 2 h in a flow of 20 vol % H_2 in He at a total flow rate of 50 mL/min. Thereafter, the sample was cooled to 350 °C and exposed to a mixture of 4% CO and 12% H_2 in He for 16 h. After cooling the spent samples to 50 °C in He, TPH was performed by flowing 20 vol % H_2 in He at a rate of 50 mL/min, while ramping the sample to 650 °C at a rate of 10 °C/min followed by a dwell of 30 min. Reactants and products during reduction and reaction were analyzed with an online mass spectrometer (Balzers TPG-300).

2.2.8. Infrared Spectroscopy (IR). *In situ* IR spectroscopy was performed on a Bruker Vertex 70v Fourier-Transform infrared spectrometer equipped with a DTGS detector and CaF_2 windows to separate the vacuum part from the environmental reaction cell. A total of 32 spectra were averaged at a resolution of 2 cm^{-1} in the spectral range between 4000 and 1000 cm^{-1}. Typically, samples were pressed into self-supporting wafers of 15 mg (diameter 13 mm) and reduced *in situ* at 450 °C using a heating rate of 5 °C/min followed by an isothermal dwell of 1 h in a 20 vol % H_2 in N_2 flow. The sample was then outgassed at 300 °C for 30 min and the temperature was lowered to 50 °C under vacuum prior to introducing probe molecules. Small amounts of CO_2 were added to the cell using a six-way valve connected with a 10 μL sample loop. IR spectra were recorded as a function of the CO_2 pressure up to 10 mbar. Temperature-programmed desorption (TPD) was employed to study the evolution and removal of adsorbed species. For this purpose, the sample was heated to 350 °C at a rate of 5 °C/min, while recording IR spectra at intervals of 25 °C. For *in situ* methanation measurements, reduced catalysts were exposed to 100 mbar of a gas mixture containing H_2 and CO_2 in a ratio of 4/1 at 50 °C. The sample was then heated to 350 °C at a rate of 5 °C/min, while recording IR spectra at intervals of 25 °C.

2.3. Catalytic Activity Measurements. *2.3.1. CO_2 Hydrogenation.* The catalytic activity in CO_2 hydrogenation was evaluated between 200 and 400 °C in a parallel ten-flow reactor setup. Typically, 50 mg of catalyst (75−125 μm sieve fraction) and 150 mg SiC were mixed and loaded in quartz reactor tubes with an internal diameter of 4 mm. Catalysts were reduced *in situ* by heating to 450 °C at a rate of 5 °C/min followed by an isothermal dwell of 4 h, in a 10 vol % H_2 in He flow of 50 mL/min. The reaction feed mixture consisted of 3 vol % CO_2, 12 vol % H_2 balanced with He. The total gas flow rate was 50 mL/min. The reaction was started at 200 °C. In a typical experiment the temperature was raised in steps of 25 °C up to 400 °C, with steady-state activities generally obtained after ca. 25 min at each temperature. Effluent products were analyzed by online gas chromatography (Interscience CompactGC) equipped with Restek Rt-Q-Bond and Rt-Msieve 5 Å (TCD), Restek Rt-U-Bond and Rt-Q-Bond (TCD), and Restek Rtx-1 (FID) columns. The CO_2 conversion (X_{CO2}) and CH_4 (S_{CH4}) and CO (S_{CO}) selectivities are calculated as

$$X_{CO2} = \frac{[CH_4] + [CO]}{[CO_2] + [CH_4] + [CO]} \quad (1)$$

$$S_{CH4} = \frac{[CH_4]}{[CH_4] + [CO]} \quad (2)$$

$$S_{CO} = \frac{[CO]}{[CH_4] + [CO]} \quad (3)$$

2.3.2. CO Hydrogenation. The catalytic activity in CO hydrogenation was determined to investigate the stability of the catalysts. For this purpose, the reaction feed for CO_2 hydrogenation was replaced by a mixture containing 4 vol % CO, 12 vol % H_2 in He at a total flow rate of 50 mL/min. Product analysis was carried out using the same online gas chromatograph as used for the CO_2 hydrogenation experiments. The CO conversion (X_{CO}) was determined as

$$X_{CO} = \frac{[CH_4] + [CO_2]}{[CO] + [CH_4] + [CO_2]} \quad (4)$$

2.3.3. Steady-State Isotopic Transient Kinetic Analysis (SSITKA). SSITKA measurements were carried out to study the intrinsic kinetics of CO_2 hydrogenation. The setup used for these SSITKA measurements has been described in more

DOI: 10.1021/acscatal.9b01968
ACS Catal. 2019, 9, 7823−7839

detail elsewhere.[63] In a typical measurement, 200 mg catalyst was loaded into the stainless-steel reactor tube after dilution with SiC. The sample was reduced by heating in a flow of 50 mL/min of 20 vol % H_2 in Ar at a rate of 5 °C/min to 450 °C followed by an isothermal dwell of 2 h. The reactor was subsequently cooled in the same gas flow to 200 °C, and the total pressure was increased to 2 bar. The SSITKA experiments were started by a forward transient switch from the 20 vol % H_2 in He mixture to a mixture of H_2, CO_2, and Ar in a volumetric composition of 8/2/40 at a total flow rate of 50 mL/min. The reaction was monitored by online gas chromatography (Thermo Scientific, Trace GC 1300). After reaching steady state, a SSITKA switch $H_2/^{12}CO_2/Ar \rightarrow H_2/^{13}CO_2/He$. The transient of $^{13}CO_2$ (m/z = 45), $^{12}CO_2$ (m/z = 44), $^{13}CH_4$ (m/z = 17), $^{12}CH_4$ (m/z = 15), and He (m/z = 4) was followed by online mass spectrometry (EES, GeneSys).

2.4. Computational Modeling. *2.4.1. Density Functional Theory Calculations.* All density functional theory (DFT) calculations were carried out using the Vienna ab initio simulation package (VASP)[64−66] with the Perdew−Burke−Ernzerhof (PBE) exchange-correlation functional.[67] The projector-augmented-wave (PAW)[68] method was used to describe the core electrons. A plane-wave cutoff energy of 400 eV was employed for the valence electrons. The geometry optimization was converged until the maximal residual force was smaller than 0.02 eV/Å, and the electronic self-consistent field was converged to 1×10^{-4} eV. The optimized crystal lattice constant of Ni is 3.525 Å, which is in very good agreement with the experimental value of 3.524 Å.[69] In order to avoid spurious interactions, a vacuum zone of at least 15 Å was set along the z-direction. Monkhorst−Pack k-point grids of $3 \times 3 \times 1$ and $3 \times 6 \times 1$ were used for Mn_4O_4−Ni(111) and Ni(311) surface calculations, respectively.[70] The Ni(111) surface slab of the Mn_4O_4−Ni(111) model consisted of three atomic layers of a $p(4 \times 4)$ unit cell. The bottom two Ni layers were fixed at the corresponding bulk positions, while the top Ni layer, and the Mn_4O_4 cluster together with the adsorbates were allowed to relax during the calculations. The Ni(311) surface was represented as eight Ni layers with a $p(2 \times 2)$ unit cell. The bottom four layers of Ni(311) surface were fixed at the bulk crystal structure, while the top four layers and the adsorbates were relaxed. To identify the most stable structure of a Mn_4O_4 cluster on the Ni(111) surface, a genetic algorithm was employed.[71] For this purpose, an initial population of 12 random starting candidates was prepared. All of these structures had reasonable Mn−O distances in the 1.7−2.9 Å range in order to avoid redundant calculations. The DFT energies of these structures were then evaluated by a fitness function[72] and new populations were then generated by crossover and mutation operations as defined by Deaven and Ho.[73,74] Structures with lower energy have a higher probability for doing a crossover operation. For mutation, rattle and twist operations were considered.[72] A fraction of 40% of the atoms in the Mn_4O_4 clusters were allowed to move at a random distance in a random direction with perturbations between −0.3 and 0.5 Å. The adsorbed cluster can be rotated at a random angle ranging from 1 to 180° with respect to the surface normal. From each generation, the four most stable structures were kept. Random numbers were generated by the Mersenne Twister random number generator. In total more than 400 structures were obtained by this approach. After 40 cycles, no further changes in the structure and energy were found anymore.

The climbing-image nudged elastic band and force reversed methods were used to determine transition states (TSs).[75−77] The force tolerance used in these calculations was 0.02 eV/Å. A frequency analysis was carried out to verify that each transition state had only one imaginary frequency along the reaction coordinate. To this end, the Hessian matrix was computed based on the finite difference approach during which adsorbates were free to relax in all directions and the metal atoms were fixed. A zero-point energy (ZPE) correction was applied to all adsorption energies, activation barriers, and reaction energies.

2.4.2. Microkinetics Simulations. Microkinetics simulations were carried out using the in-house developed MKMCXX code,[78] which has been extensively employed in previous works to investigate CO hydrogenation on Rh and Ru surfaces.[79−81] The most important assumptions underlying the computation of adsorption, desorption, and reaction rate constants are given in the Supporting Information. In this work, we implemented an isobaric and isothermal continuously stirred tank reactor (CSTR) model, assuming that the gases behave ideally. Gas-phase concentrations C_i were determined according to (eq 5), where r_i is the production or consumption of species i on a single active site.

$$V \frac{dC_i}{dt} = F_i^{in} - F_i^{out} + N_{sites} \times r_i \quad (5)$$

The flow rates F_i^{in} at the reactor entrance were chosen to obtain a residence time of 1 s at differential conditions. The reactor was operated at isobaric conditions.

2.5. Reactor Modeling. A Sabatier reactor was modeled as a one-dimensional heterogeneous plug-flow reactor (PFR) model.[82] As this reaction can suffer from significant diffusion limitations in the hotspot,[83] the reactor was modeled with canonical mass and energy balances in which interfacial and intraphase mass and heat transfer was considered. The details thereof are outlined in detail in the Supporting Information. The pressure drop along the axial coordinate of the reactor was neglected and the ideal gas assumption was applied. Heat exchange to the external environment was neglected and the reactor was cooled with an isothermal cooling stream fixed at 200 °C with a given heat transfer coefficient. For the modeling of the Ru/Al_2O_3 system, the kinetic model by Falbo et al.[84] was used. For the modeling of the Ni and NiMn systems, the original kinetic model for $Ni/MgAl_2O_4$ by Xu and Froment[85] was adapted to describe available experimental data for optimum catalysts. The inlet stream was composed of H_2 and CO_2 in a 4:1 molar ratio with no dilution at a pressure of 10 bar and a gas hourly space velocity of 3000 h^{-1}. The mass and heat balance equations were solved using Matlab.

3. RESULTS AND DISCUSSION

3.1. Characterization. The basic physicochemical properties of the catalyst samples are summarized in Table 1. ICP elemental analysis shows that all samples contain approximately 3 wt % Ni with Ni/Mn atomic ratios between 0.5 and 2 as intended. The XRD patterns of the as-prepared samples contain only diffraction lines that can be assigned to the anatase and rutile forms of TiO_2 (Supporting Information, Figure S1). This implies that the Ni and Mn precursors are either present in an amorphous phase or as very small crystallites.

Catalyst reducibility was initially studied with H_2-TPR. All Ni-containing catalysts can be reduced below 450 °C

DOI: 10.1021/acscatal.9b01968
ACS Catal. 2019, 9, 7823−7839

Table 1. Metal Loadings As Determined with ICP, Particle Sizes Determined by STEM-EDX, and Available Active Sites Determined by CO Chemisorption

sample	Ni (wt %)	Mn (wt %)	Ni/Mn	d (nm)	CO chem (μmol/gcat)
Ni	2.9	0	n/a	5.7	47.0
NiMn(2:1)	2.8	1.4	1.9	6.4	44.8
NiMn(1:1)	2.9	2.7	1.0	5.2	33.9
NiMn(1:2)	2.6	4.9	0.5	6.6	30.8
Mn	0	2.8	n/a		

(Supporting Information, Figures S2 and S3). The traces for Ni/TiO_2 contain reduction peaks at 300 and 325 °C, which are both attributed to Ni^{2+} reduction to Ni^0. The feature at higher temperature is associated with Ni^{2+} species in stronger interaction with TiO_2. In comparison with Ni/TiO_2, the $NiMn(2:1)/TiO_2$ sample showed a higher H_2 consumption in the 250−300 °C range which is, as we will confirm later, due to the simultaneous reduction of Mn^{3+} to Mn^{2+} and weakly interacting Ni^{2+} to Ni^0. Increasing the Mn content for $NiMn(1:1)/TiO_2$ and $NiMn(1:2)/TiO_2$ results in a shift of the Ni reduction peaks to higher temperature. The sample containing only Mn could not be reduced, even at a temperature of 900 °C.

In order to gain a more detailed insight into the size and distribution of Ni and Mn phases over the TiO_2 surface, we analyzed the reduced samples by dark-field STEM with elemental mapping (STEM-EDX). Figure 1 shows representative images and EDX maps of reduced $NiMn(2:1)/TiO_2$, $NiMn(1:1)/TiO_2$, and $NiMn(1:2)/TiO_2$ samples (images for other samples in the Supporting Information). The EDX maps of reduced samples confirm that the Ni-containing samples consist of Ni nanoparticles. We determined mean particle sizes of 5.7 nm for Ni/TiO_2 (Supporting Information, Figure S5), 5.2 nm for $NiMn(2:1)/TiO_2$, 6.4 nm for $NiMn(1:1)/TiO_2$, and 6.6 nm for $NiMn(1:2)/TiO_2$. The EDX maps show that Mn was distributed much better over the TiO_2 support than Ni after reduction at 450 °C. To assess how Ni and Mn distribution changed during reduction, EDX maps of dried Ni/TiO_2 and $NiMn(1:1)/TiO_2$ samples were obtained prior to reduction. Figure 2 shows the EDX maps of Ti, O, Ni, and Mn of $NiMn(1:1)/TiO_2$ before reduction. Ni and Mn EDX maps show considerable overlap. We therefore conclude that Ni and Mn have an affinity toward each other, possibly forming a mixed NiMn oxide when dried. Such crystallites are likely small or amorphous since no XRD reflection peaks were observed. In addition, STEM-EDX measurements of $NiMn(1:1)/TiO_2$ after reduction obtained at higher magnification (Supporting Information, Figure S6) show the particles are partially decorated by Mn. In the absence of Mn, the Ni precursor was found to be distributed homogeneously on the TiO_2 support (Supporting Information, Figure S7). This demonstrates that, during reduction, the Ni becomes mobile on the TiO_2 and aggregates to form nanoparticles. In contrast, the Mn

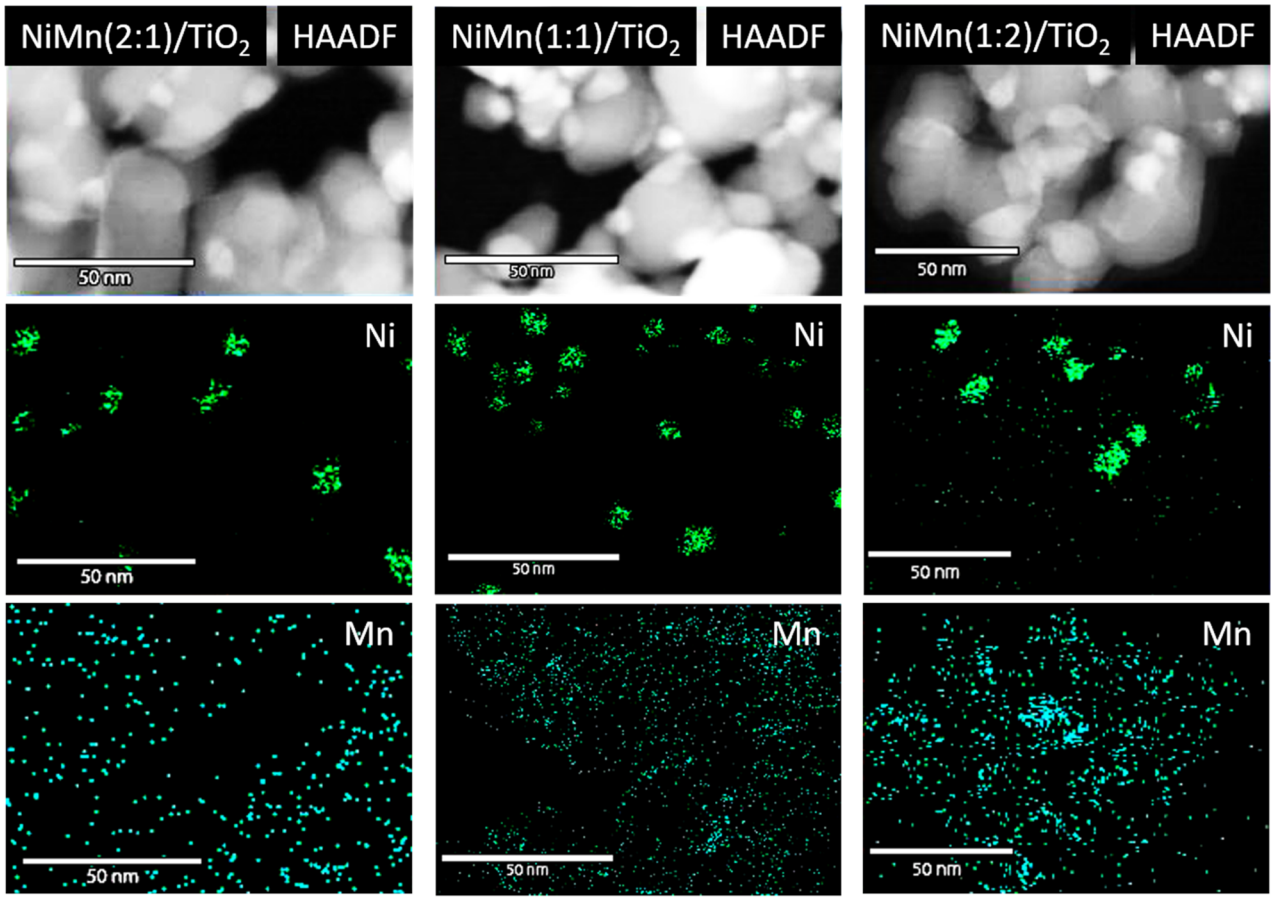

Figure 1. HAADF-STEM with corresponding EDX mapping showing localized Ni particles and dispersed Mn over the entire support after reduction at 450 °C.

DOI: 10.1021/acscatal.9b01968
ACS Catal. 2019, 9, 7823−7839

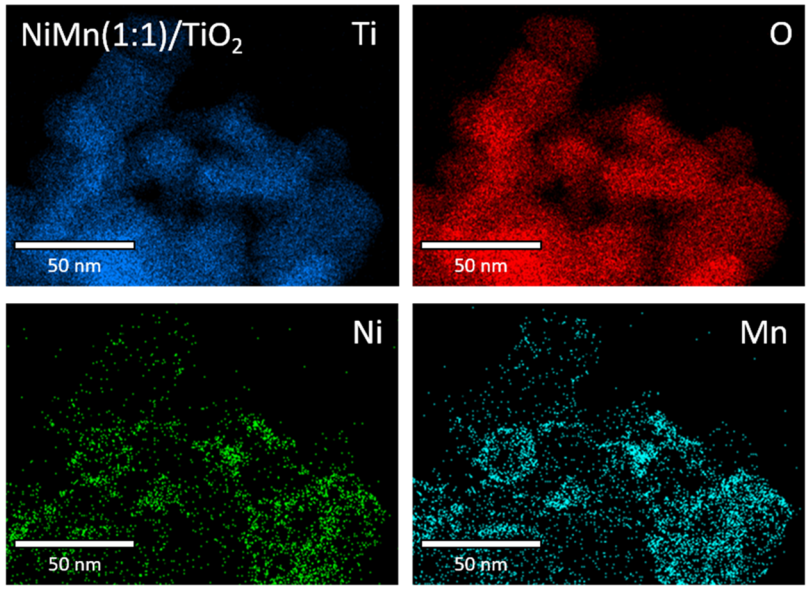

Figure 2. STEM-EDX mapping of unreduced NiMn(1:1)/TiO_2 catalyst after drying at 110 °C. The EDX maps of Ni (green) and Mn (turquoise) demonstrate a clear affinity between Ni and Mn before reduction and indicate a highly dispersed mixed NiMn oxide phase.

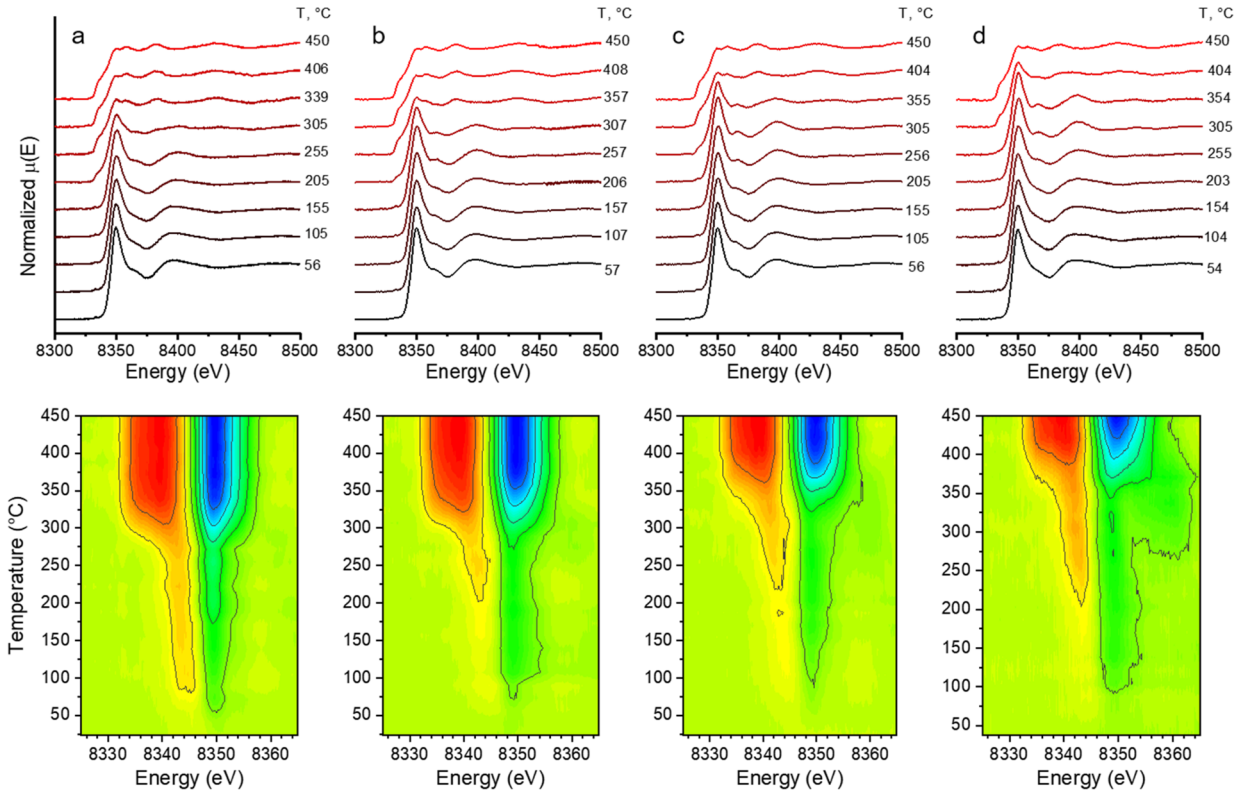

Figure 3. *In situ* XANES spectra at the Ni K-edge of (a) Ni/TiO_2, (b) NiMn(2:1)/TiO_2, (c) NiMn(1:1)/TiO_2, and (d) NiMn(1:2)/TiO_2, highlighting the delayed onset of reduction with increased Mn loading. Corresponding difference spectra shown below show the shift of the edge to lower binding energies (red) and the decrease in the white line (blue) during the reduction process. The onset of reduction is clearly delayed with increasing ratios of Mn.

remains well dispersed, suggesting a strong interaction with the support.

Chemisorption measurements show a clear decrease in CO uptake with increasing Mn content for the samples reduced at 450 °C. This shows that Mn addition led to an increase in the Ni particle size or a partial coverage of metallic Ni by Mn. Combined with the mean particle sizes determined by HAADF-STEM, we conclude that Mn partially covers the reduced Ni surface. Such a type of interaction has been reported before when oxidic Mn interacts with reduced Co nanoparticles.[86]

In a successive step, we investigated the reduction of Ni and Mn in more detail by *in situ* XANES. Ni K-edge XANES spectra collected during reduction between 50 and 450 °C are

DOI: 10.1021/acscatal.9b01968
ACS Catal. 2019, 9, 7823−7839

presented in Figure 3. These data show that Ni in these samples started with the oxidation state of 2+ (also confirmed by XPS, see Figure S4 in the Supporting Information) and is entirely reduced to Ni^0 by 450 °C. The Ni reduction progress can be appreciated from the difference spectra contours (obtained by subtracting the room temperature spectrum from the higher temperature spectra) that reflect a decrease in the whiteline (i.e., sharp edge-jump feature, highlighted in blue on contour plot) and the shift of the edge to lower energies (in red). The addition of Mn increased the temperature at which full reduction was achieved from 300 °C for Ni/TiO_2 to just above 400 °C for $NiMn(1:2)/TiO_2$. The lower reducibility of Ni in the bimetallic samples can be explained by a Ni−Mn interaction. XANES measurements on the Mn K-edge reveal that Mn remained in the +2 oxidation state throughout the reduction treatment for Mn/TiO_2 (Supporting Information, Figure S8), consistent with the TPR finding that hydrogen was not consumed during H_2-TPR of this sample (Supporting Information, Figure S2). Differently, we observe that Mn is present as a mixed Mn^{3+}/Mn^{2+} oxide in the Ni-containing samples. As oxidation of the Mn^{2+} precursor by TiO_2 could be excluded on the basis of XPS data (Supporting Information, Figure S4), we conclude that the mixed valency of Mn is due to the formation of a mixed oxide phase between Ni and Mn during drying. The shift in the whiteline to 6554 eV in the XANES spectra demonstrates that Mn^{3+} is reduced to Mn^{2+} between 250 and 300 °C. The corresponding Ni XANES data evidence that part of the Ni^{2+} in the precursor was reduced to metallic Ni in the same temperature range, explaining the higher hydrogen consumption during H_2-TPR of the NiMn samples. It is likely that this first Ni reduction peak facilitates the reduction of Mn^{3+} to Mn^{2+} via hydrogen spillover, further suggesting that this form of Ni^{2+} that weakly interacts with titania is closely located to Mn in the oxidic precursor.[87] Overall, we can conclude that Ni is present as metallic particles, which are partially covered by MnO particles. MnO is also present in high dispersion on the titania support.

Structural information on the catalysts was obtained by analyzing the recorded EXAFS data. The k^3-weighted R-space spectra (not phase corrected) are plotted in Figure 4. A characteristic Ni−O contribution is observed at 2.08 Å before reduction. A small contribution of Ni−Ni at 3.12 Å, typical for Ni in $Ni(OH)_2$, can also be seen for all unreduced samples. The low second shell coordination numbers derived from these spectra confirm that, prior to reduction, Ni is dispersed well as the oxide. Following reduction at 450 °C, the Ni−O coordination shell has completely disappeared. First-shell fitting showed a Ni−Ni contribution at 2.49 Å, which is characteristic of metallic Ni. The corresponding coordination numbers for reduced Ni/TiO_2 and $Ni:Mn/TiO_2$ samples are comparable (Table 2), suggesting that the Ni dispersion in these samples is not too different, which is in line with the TEM results. A full overview of the fit results is reported in the Supporting Information (Table S3). As commonly observed for metal oxides, it was not possible to fit the EXAFS data obtained at the Mn K-edge for the fresh and reduced samples in a satisfactory manner. Based on the exclusive presence of Mn^{2+} derived by XANES and the Ni EXAFS data analysis, we can exclude the formation of reduced bimetallic NiMn particles.

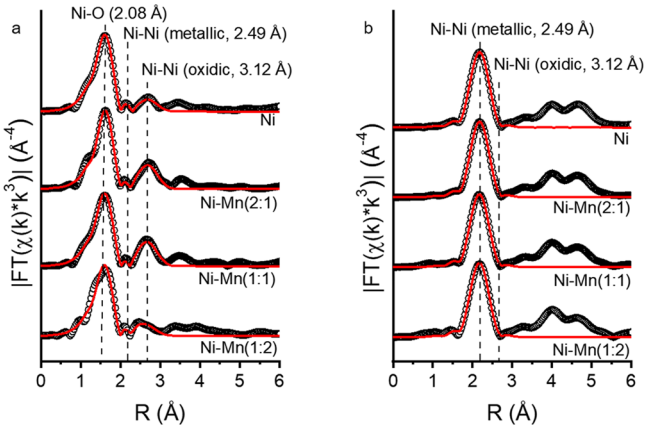

Figure 4. k^3-Weighted R-space plots of NiMn catalysts (a) before and (b) after reduction at 450 °C.

Table 2. Ni K-Edge EXAFS Fitted Coordination Numbers for Ni and NiMn Catalysts with Varying Mn/Ni Ratios and after Varying Treatments[a]

		coordination number	
sample name	treatment	Ni−O (±)	Ni−Ni (±)
Ni	fresh	6.6 (0.4)	1.4 (0.9)
	H_2, 450 °C		10.9 (0.3)
	CO_2/H_2, 350 °C		10.1 (0.4)
	CO/H_2, 350 °C		9.9 (0.4)
NiMn(2:1)	fresh	5.7 (0.6)	3.7 (1.7)
	H_2, 450 °C		10.8 (0.2)
NiMn(1:1)	fresh	6.5 (0.4)	4.0 (1.1)
	H_2, 450 °C		9.9 (0.3)
NiMn(1:2)	fresh	6.2 (0.5)	3.4 (2.9)
	H_2, 450 °C		10.3 (0.6)
	CO_2/H_2, 350 °C		10.2 (0.5)
	CO/H_2, 350 °C		9.7 (0.3)

[a]Error margins are reported in brackets.

3.2. Catalytic Activity Measurements. We then determined the performance of the different reduced samples in the Sabatier reaction (Figure 5). Figure 5a and b show the CO_2 conversion and CO selectivity as a function of the reaction temperature. The Mn/TiO_2 catalyst is not active in CO_2 methanation. The conversion profiles for the other catalysts show a typical Arrhenius behavior with the CO_2 conversion approaching the thermodynamic equilibrium above 350 °C. The $NiMn/TiO_2$ samples are substantially more active than Ni/TiO_2. The activity increases with the Mn content. Turnover frequencies (TOFs) calculated at 250 °C show that the most active NiMn sample is nearly 6 times more active than the Ni/TiO_2 sample (Table 3). The performances of $NiMn(1:1)/TiO_2$ and $NiMn(1:2)/TiO_2$ are very similar, suggesting that the optimum Ni/Mn ratio is already reached at an equimolar Ni/Mn ratio. Moreover, these TOFs compare favorably with those reported in the literature for Ni-based catalysts under similar conditions (Supporting Information, Table S4). The CO selectivity of the Ni:Mn samples is higher than that of Ni/TiO_2 at intermediate temperatures. This difference suggests a role of Mn in the activation of CO_2 to CO, which is often considered as an intermediate in the Sabatier reaction. We also observed a significant difference in the overall kinetics of the reaction. Higher apparent activation energies of ∼75 kJ/mol were determined for the NiMn samples than the value of 59 kJ/mol for Ni/TiO_2 (Table 3).

DOI: 10.1021/acscatal.9b01968
ACS Catal. 2019, 9, 7823−7839

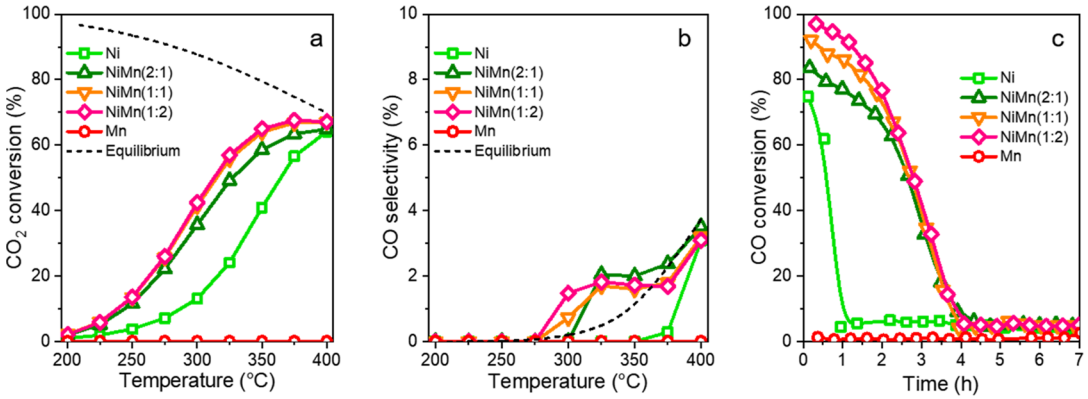

Figure 5. CO_2 methanation: (a) steady-state CO_2 conversion and (b) CO selectivity of $NiMn/TiO_2$ catalysts as a function of the temperature (H_2/CO_2 = 4, 3 vol % CO_2, 50 mL/min, 1 atm). (c) CO methanation at 350 °C as a function of time on stream (H_2/CO = 3, 4 vol % CO, 50 mL/min, 1 atm).

Table 3. Activation Barriers and TOFs Based on Methane Formation

sample	E_a^{app} (kJ/mol)[a]	TOF (10^{-2} mol CH_4/mol $Ni_{surface}$/s)[b]
Ni	59 (±2)	1.1
NiMn(2:1)	74 (±1)	3.5
NiMn(1:1)	75 (±1)	5.2
NiMn(1:2)	77 (±1)	5.9
Mn	n/a	n/a

[a]The apparent activation energy determined for CO_2 conversions lower than 20%. [b]Surface Ni amount determined by CO chemisorption assuming a stoichiometric ratio CO/Ni = 1.5. TOF computed based on CO_2 conversions at 250 °C.

Mechanistically, CO_2 hydrogenation is thought to follow the reverse water−gas shift reaction of CO_2 to CO, which is then converted to CH_4.[48] The higher than equilibrium CO selectivity for the more active NiMn catalysts indicates that the reaction from CO_2 to CO benefits more from Mn promotion than the second CO hydrogenation step to CH_4. It has already been reported before that CO_2 dissociation is enhanced in the presence of oxophilic sites.[88] Accordingly, we speculate that Mn plays a role in CO_2 dissociation reactions. The origin of the higher measured activation energy will be discussed in the theoretical modeling section below.

We observed that the catalysts were stable for 35 h during CO_2 methanation at 350 °C (Supporting Information, Figure S10), although the Ni/TiO_2 showed a slight activation over time, likely due to a stronger metal−support interaction. Instead of studying long-term stability of these catalysts in the Sabatier reaction, we investigated their stability under more demanding conditions, i.e., in CO methanation using a feed with a H_2/CO ratio of 3 at a temperature of 350 °C. It is known that CO methanation leads to faster buildup of coke, which can deactivate the catalyst.[29] The trends in initial CO conversion (Figure 5c) correlate with the Mn content in a similar way as the CO_2 conversion. This shows that the presence of Mn also improves the hydrogenation of CO to CH_4. We observe that CO methanation led to deactivation of all the catalysts but that deactivation started later for the $NiMn/TiO_2$ samples. We verified by TPH that deactivation was due to the buildup of coke deposits on the catalyst surface. Catalysts operated in CO methanation for 16 h were exposed to a H_2 feed, while raising the temperature from 50 to 650 °C. The resulting traces (Supporting Information, Figure S11) contain a CH_4 formation feature at relatively high temperature, consistent with the hydrogenation of graphitic carbon on Ni.[89] The TPH profiles show that the spent Ni/TiO_2 sample contained much more carbon deposits than the spent $NiMn/TiO_2$ samples, in line with the higher stability of the Mn-promoted catalysts in CO methanation. Accordingly, we can conclude that the addition of Mn improved the catalytic activity and also the resistance to carbon poisoning. As it is usually assumed that CO dissociation is the slow step in CO methanation on Ni catalysts, these findings also suggest that Mn also promotes CO dissociation. The selectivity will depend on the rate of hydrogenation to CH_4 vs carbon−carbon coupling reactions that lead to coke. Another role of Mn-oxide might be the suppression of formation of carbidic carbon on Ni. Enhanced resistance to coking was also reported in Mn-promoted Ni/Al_2O_3 catalysts used for dry methane reforming.[90] Evidently, this kind of deactivation does not take place during CO_2 methanation, which can be explained by the low conversion rate of CO_2 to CO, which prevents buildup of carbon species on the Ni surface. This is in line with the much lower rate of CH_4 formation in CO_2 methanation than in CO methanation.

Taking into account the results from our nanoscale characterization, we conclude that the active phase in the reduced $NiMn/TiO_2$ catalysts is made up of metallic Ni nanoparticles in contact with MnO. Clearly, both CO_2 and CO bond dissociation benefit from the presence of an interface between metallic Ni and MnO. The Ni−Mn interaction is already present in the oxidic precursor and most likely evolves via reduction of Ni^{2+} into Ni^0 particles with the MnO ending up partly on the metallic Ni particles. Evidently, only a fraction of Mn is in contact with Ni, the remainder being dispersed on the titania support. Although the Ni particle size slightly increases with Mn content, which may be due to a slightly lower interaction with TiO_2 due to the presence of MnO competing for reactive support surface sites, we consider that the higher activity in CO_2 and CO methanation is mainly due to a change in the quality of the active sites at the Ni surface and relates to an interface created with the MnO phase.

3.3. Mechanistic Investigations. *3.3.1. In situ IR Spectroscopy.* Although CO_2 methanation has been extensively studied, the reaction mechanism remains heavily debated. In general, two mechanisms are discussed: (i) CO_2 dissociation to yield a CO intermediate with subsequent CO methanation and (ii) direct CO_2 hydrogenation toward CH_4

DOI: 10.1021/acscatal.9b01968
ACS Catal. 2019, 9, 7823−7839

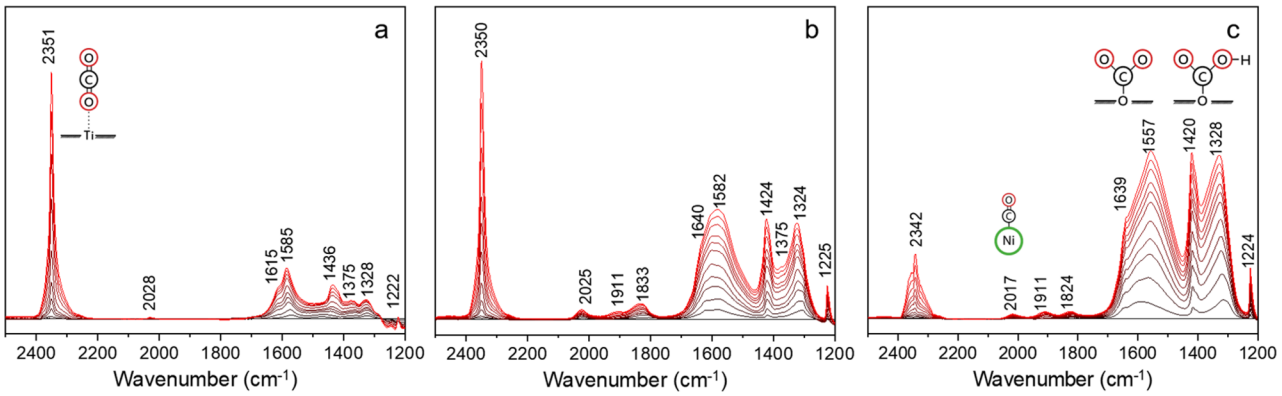

Figure 6. IR spectra after CO_2 adsorption at 50 °C with increasing pressure from 0 to 10 mbar on reduced (a) Ni/TiO_2, (b) $NiMn(2:1)/TiO_2$, and (c) $NiMn(1:2)/TiO_2$ samples.

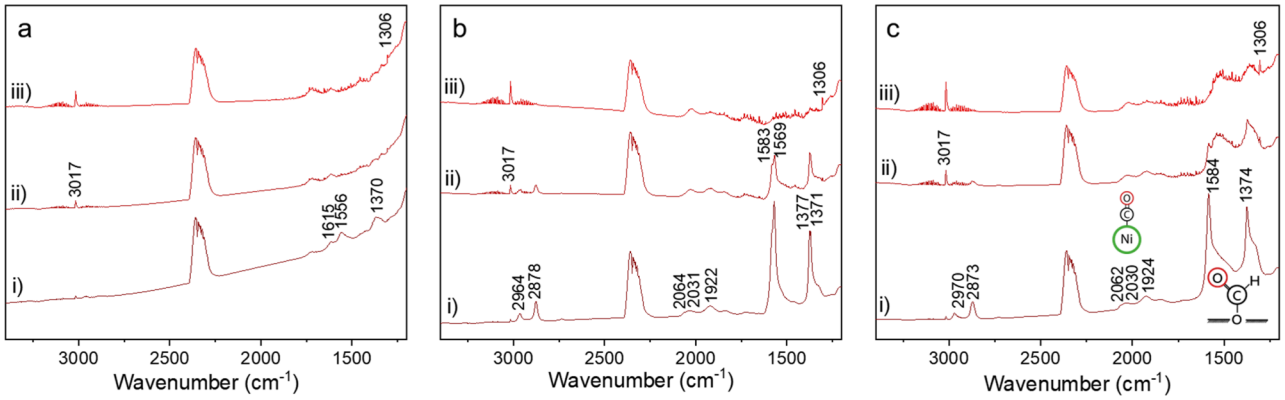

Figure 7. IR difference spectra for (a) Ni, (b) $NiMn(2:1)/TiO_2$, and (c) $NiMn(1:2)/TiO_2$ obtained under CO_2 methanation conditions between at (i) 200 °C, (ii) 250 °C, and (iii) 300 °C (H_2/CO_2 = 4, 100 mbar).

without formation of a CO surface intermediate.[46,47] The CO intermediate in the first mechanism may either be formed through direct CO_2 dissociation[40,41] or via formate species.[42−45] Recent studies on Ni-based catalysts have highlighted the influence of the Ni particle size[36] and the support on these CO_2 methanation pathways.[41,46,91] The observed surface intermediate species were found to strongly depend on the basicity of the support.[92] To better understand the role of possible reaction pathways for the Ni and NiMn catalysts, we investigated these samples by *in situ* IR spectroscopy.

Figure 6 shows the different IR spectra obtained at increasing CO_2 coverage for the samples reduced at 450 °C. The spectra obtained for $NiMn(2:1)/TiO_2$ at 50 °C contain clear signatures of linear, bridged and 3-fold-coordinated CO (carbonyl) species on metallic Ni (2025, 1911, and 1833 cm^{-1}, respectively). Similar bands were slightly red-shifted for $NiMn(1:2)/TiO_2$ (2017, 1911, and 1824 cm^{-1}, respectively), suggesting that the carbonyl bond was weakened by the addition of Mn. Compared to these clear carbonyl bands, only a very minor feature of linear CO was observed on Ni/TiO_2. These substantial differences between Ni/TiO_2 and its Mn-promoted counterparts evidence the more facile activation of CO_2 at a very low temperature. The appearance of carbonyl bands on metallic Ni further suggests that CO_2 is activated at the interface between Ni and MnO, with the CO product strongly adsorbing to the metal surface.

The IR spectra of adsorbed CO_2 also contain information about the support basicity. Ni/TiO_2 exhibited primarily linearly adsorbed CO_2 at 2351 cm^{-1} with minor contributions of carbonates (1585, 1436 cm^{-1}) and bicarbonates (1420, 1222 cm^{-1}). In contrast, CO_2 adsorption on $NiMn(2:1)/TiO_2$ led to more bicarbonates (1640, 1424, 1225 cm^{-1}) and carbonates (1582, 1324 cm^{-1}). At higher Mn content, the amount of bicarbonates (1639, 1420, 1224 cm^{-1}) and carbonates (1557, 1328 cm^{-1}) increased, while the signal of linearly adsorbed CO_2 (2442 cm^{-1}) became very weak. These results can be explained by the higher basicity of MnO in comparison to TiO_2.[90] Thus, the interaction of CO_2 with MnO leads to (bi)carbonates, which is further confirmed by the IR spectra obtained during CO_2-TPD between 50 and 350 °C. The adsorption strength of CO_2 probed in this manner follows CO_2 linear < bicarbonate < carbonate (Supporting Information, Figure S12).

We also investigated these three catalysts by IR spectroscopy in the presence of the reaction mixture used for CO_2 methanation (H_2/CO_2 = 4, 100 mbar) in the 50−350 °C temperature range. Figure 7 shows that Ni/TiO_2 contains weak features of carbonates below 100 °C and minor contributions of formates between 100 and 200 °C (1556, 1359 cm^{-1}), while CH_4 formation starts at 200 °C as evident from the characteristic gas-phase CH_4 bands at 3017 and 1306 cm^{-1}. In contrast, both $NiMn(2:1)/TiO_2$ and $NiMn(1:2)/TiO_2$ show considerable (bi)carbonate contributions between 50 and 100 °C (Supporting Information, Figure S13). Increasing the temperature above 100 °C led to the appearance of bands at 2873 (ν(CH)), 1584 ($\nu_{as}(CO_2^-)$), and 1374 cm^{-1} ($\nu_s(CO_2^-)$) for $NiMn(1:2)/TiO_2$, which can be assigned to formate. The corresponding spectra for $NiMn(2:1)/TiO_2$

DOI: 10.1021/acscatal.9b01968
ACS Catal. 2019, 9, 7823−7839

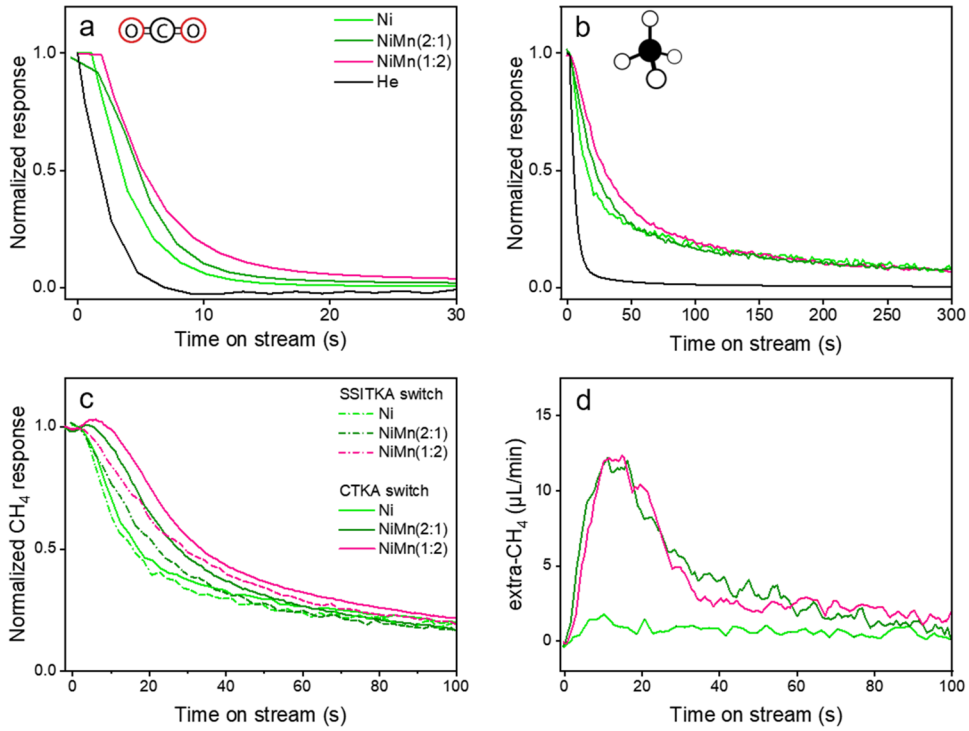

Figure 8. Response of (a) CO_2 (reactant) and (b) CH_4 (product) after the SSITKA ($^{12}CO_2/H_2/Ar \rightarrow {}^{13}CO_2/H_2/He$) switch. (c) Normalized CH_4 residual response of the SSITKA switch and CTKA ($CO_2/H_2/He \rightarrow H_2/He$) switch. (d) Presence of excess surface carbon after the CTKA switch to H_2/He. Excess surface carbon is determined from the difference in CH_4 flows between CTKA and SSITKA experiments, expressed as extra-CH_4.

show a splitting in the vibrations at 1583 and 1569 cm^{-1} ($\nu_{as}(CO_2^-)$) and 1377 and 1371 cm^{-1} ($\nu_{as}(CO_2^-)$), respectively. This splitting of CO_2^- vibrations suggests that the type of formate species depends on the MnO content.[93] We also observed significant contributions from adsorbed carbonyls on NiMn catalysts above 200 °C, a species which was absent from Ni/TiO_2 spectra. This recurring characteristic further supports our hypothesis that CO_2 activation is enhanced over NiMn catalysts. In addition to linear (2030 cm^{-1}) and bridged (1924 cm^{-1}) species, a shoulder around 2062 cm^{-1} is indicative of di- or tricarbonyls on highly undercoordinated Ni atoms.[94] The addition of MnO to the surface provides medium basic sites compared to weakly basic TiO_2, which explains the higher CO_2 adsorption. It has been suggested that medium basic sites can promote CO_2 methanation.[92] Thus, the presence of MnO may shift the mechanism from a direct mechanism in which CO_2 is converted to CO to one where also bicarbonate/formate species play a role. We will return to this issue when exploring possible reaction mechanisms using DFT below.

3.3.2. Transient Kinetic Analysis. Figures 8a and b show the CO_2 and CH_4 responses, respectively, to a $^{12}CO_2/H_2/Ar \rightarrow {}^{13}CO_2/H_2/He$ switch at steady state at 200 °C. The quick disappearance of the He signal evidence the small gas hold-up of the system as discussed in an earlier work.[63] The much slower disappearance of the $^{12}CO_2$ signal therefore indicates a reversible interaction of CO_2 with the catalyst. The mean residence time of CO_2 became longer with increasing Mn content, demonstrating that CO_2 interacts strongly with the Mn component (Table 4). This interpretation is underpinned by the longer residence time when the switch was applied for the Mn/TiO_2 sample (Supporting Information, Figure S14). As the residence time for the NiMn/TiO_2 sample was longer than the residence time for both Ni/TiO_2 and Mn/TiO_2, there must be a role of the Ni−MnO interface in strongly adsorbing CO_2. The residence time for CH_4 was substantially longer than that of CO_2, which is due to the slow kinetics in the conversion of CO_2 to CH_4. There is also a small delay of the $^{12}CH_4$ signal for the Mn-promoted samples, despite the observed increase in methanation activity in the presence of Mn. This can suggest that the higher conversion is due to a different reaction mechanism, in agreement with the change in the apparent activation energy. The CH_4 residence time did not change much with the Mn/Ni ratio, indicating a nearly constant intrinsic methanation activity per active site.[95]

Table 4. SSTIKA Conversions, Selectivities, and Mean Residence Times of Reactants and Products for Ni and NiMn Catalysts at 200 °C

catalyst	X_{CO2} (%)	S_{CH4} (%)	$\tau(CO_2)$ (s)	$\tau(CH_4)$ (s)
Ni	1.8	99.3	3.8	84.9
NiMn(2:1)	3.1	99.4	8.6	90.3
NiMn(1:2)	3.7	99.6	11.5	89.7
Mn	0	0	7.0	n/a

The possible presence of low-reactive carbon-containing species was investigated by combining SSITKA with a backward chemical transient kinetic analysis (CTKA).[63] Specifically, the $^{12}CH_4$ transient from a $CO_2/H_2/He \rightarrow H_2/He$ is compared to the $^{12}CH_4$ transient from SSITKA ($^{12}CO_2/H_2/Ar \rightarrow {}^{13}CO_2/H_2/He$, Figure 8c). By applying a $CO_2/H_2/He \rightarrow H_2/He$ switch (Figure 8d), we observed that the surface of the NiMn/TiO_2 contains a reservoir of carbon-containing species, which is absent for Ni/TiO_2. IR spectroscopy under reaction conditions shows that the surface of the NiMn/TiO_2 catalysts contains abundant formate species, which are not

DOI: 10.1021/acscatal.9b01968
ACS Catal. 2019, 9, 7823−7839

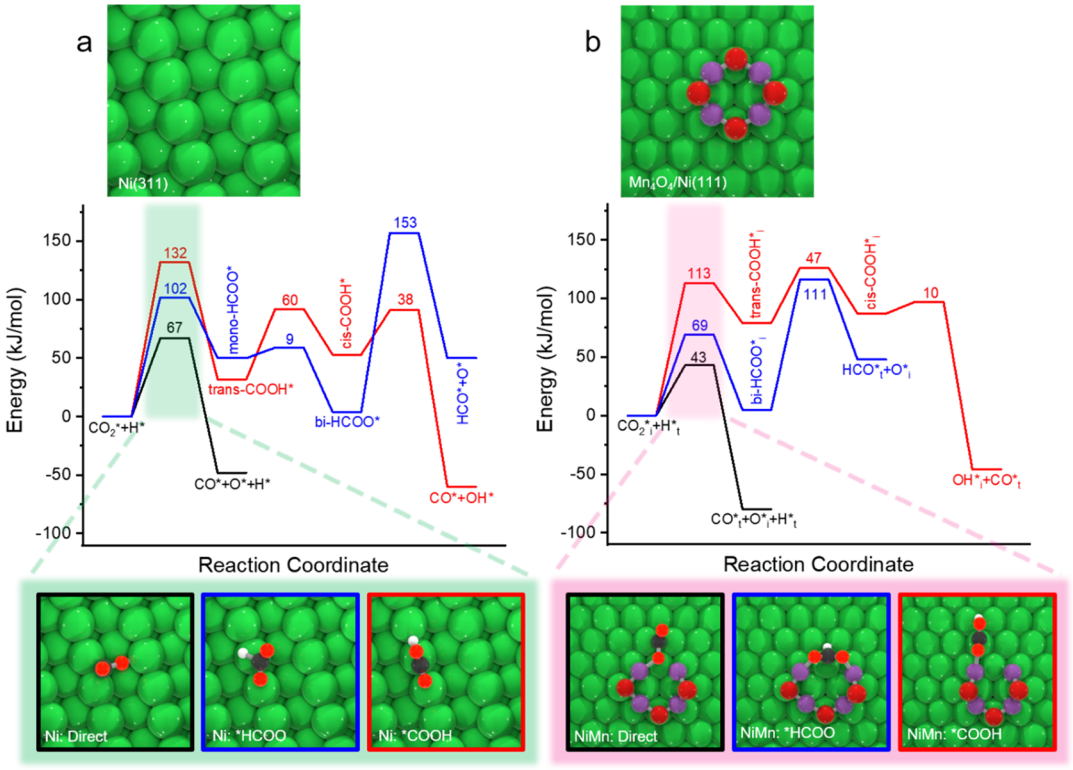

Figure 9. Models, potential energy diagrams, and transition states for the DFT calculations of the conversion of CO_2 to CO for (a) the Ni(311) surface and (b) the Mn_4O_4/Ni(111) model: (top) orthographic views of the surface unit cells, (middle) potential energy surfaces for CO_2 activation via a direct mechanism (black), a HCOO mechanism (blue) and a COOH mechanism (red), and (bottom) relevant transition states for the first step in CO_2 conversion for the three routes.

observed for Ni/TiO_2. Accordingly, we speculate that the residual surface carbon-containing species are formate species. As these species are slowly consumed during the CTKA, we infer that formate species are not part of the main reaction pathway in the conversion of CO_2 to CH_4.

3.4. Theoretical Modeling. The Ni and NiMn models used to study the mechanism of the Sabatier reaction are shown in the top panel in Figure 9. For Ni, we adopted the stepped Ni(311) surface, because step-edge sites are preferred for cleaving C−O bonds in comparison to planar surfaces. Van Helden and co-workers predicted that step-edge sites are most abundant on *fcc* nanoparticles with a size of around 6 nm,[96] in good correspondence with experimental indications for Co.[97] The Ni particles in our study have a size close to this optimum. The importance of undercoordinated Ni atoms for CO_2 activation is also evident from the literature.[98,99] The NiMn model consisted of a small Mn_4O_4 cluster placed on the Ni(111) surface.

Two main mechanisms can be distinguished for CO_2 conversion to CH_4. In the most often discussed one, CO is a surface intermediate formed by direct C−O bond scission in adsorbed CO_2 or via formate. The second mechanism involves hydrogenation of CO_2 to intermediates in which the C−O bonds are cleaved at a later stage. Figure 9 shows the potential energy diagrams and relevant transition state structures for the different pathways for CO_2 activation on the two surface models (other transition states in the Supporting Information). The preferred mode of CO_2 activation on Ni(311) is by direct C−O bond cleavage. The corresponding barrier of 67 kJ/mol is much lower than barriers of 153 and 132 kJ/mol for formate (HCOO) and carboxyl (HOCO) pathways, respectively. Once CO is formed, the reaction proceeds by CO dissociation at the step-edge and C and O hydrogenation to respectively CH_4 and H_2O. Relevant structures are provided in the Supporting Information. The lower reactivity of Ni compared to Co results in a relatively high barrier for direct C−O bond cleavage in CO on the step-edge site (166 kJ/mol *cf.* 103 kJ/mol for stepped Co).[100] As a consequence, we explored also alternative H-assisted pathways, which show that pathways involving HCO and COH with overall barriers of 180 and 149 kJ/mol, respectively, compete with the direct mechanism. As expected, C and O hydrogenation are facile on Ni.

For Mn_4O_4/Ni(111), we included more surface intermediates as CO_2 can react with the basic oxygen atoms of the Mn_4O_4 cluster. This leads to a monodentate CO_3^{2-} intermediate, which can convert to a bidentate CO_3^{2-} intermediate (Supporting Information, Table S5) and bicarbonate (HCO_3^-) after hydrogenation. These species were observed by IR spectroscopy after exposure of the NiMn catalyst to CO_2 or CO_2/H_2 at relatively low temperature. C−O bond cleavage in these species always results in adsorbed CO_2 close to the reformed Mn_4O_4 cluster and, therefore, does not give rise to CO formation.

CO formation can take place, when CO_2 is adsorbed on a partially reduced Mn_4O_4 cluster. One of the oxygen atoms of the Mn_4O_4 cluster can be hydrogenated in two steps to adsorbed H_2O (potential energy diagram given in the Supporting Information). After H_2O desorption, CO_2 can strongly adsorb at the interface, with one of the O atoms of CO_2 filling the oxygen vacancy of the Mn_4O_3 cluster. C−O bond dissociation from this state is very facile with an activation energy of 43 kJ/mol. H-assisted pathways are much

DOI: 10.1021/acscatal.9b01968
ACS Catal. 2019, 9, 7823−7839

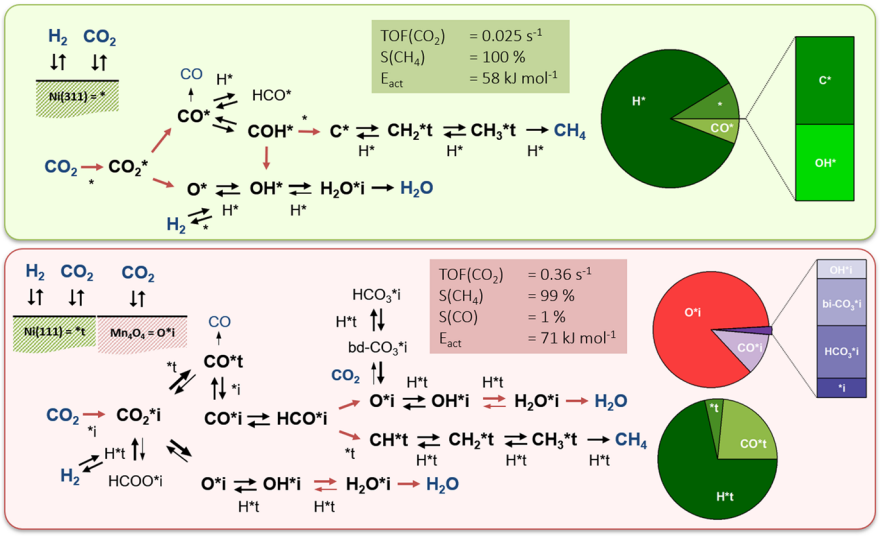

Figure 10. Microkinetics simulations based on DFT-computed reaction energetics for CO_2 methanation on (top) Ni(311) and (bottom) Mn_4O_4/Ni(111). The simulations are carried out for a temperature of 250 °C and a H_2/CO_2 ratio of 4. The composition of the surface adsorbed layer is indicated in pie-charts on the right. The main reaction pathways are also sketched with reactants and products in blue and surface intermediates in black. The use of red arrows refers to rate-controlling steps, reverse arrows indicate that reverse reactions are non-negligible (bd-CO_3 = bidentate CO_3^{2-}; HCO_3 = bicarbonate).

more difficult and, therefore, likely not relevant in the overall reaction on this surface. Nevertheless, the reaction energy diagram in Figure 9 reveals that formate (HCOO) formed upon hydrogenation of adsorbed CO_2 is a relatively stable surface intermediate and this species might be present in the IR spectra recorded in a CO_2/H_2 mixture at reaction temperature. The reaction energy diagram shows that formate is a spectator species as the barrier for its conversion to HCO is higher than the pathway to reform CO_2 followed by direct C−O bond cleavage. This supports the interpretation that formate is part of the pool of low-reactive carbon-containing surface intermediates probed by combining SSITKA and CTKA data (Figure 8).

Following CO_2 dissociation, CO can also be adsorbed at the Ni(111)−Mn_4O_3 interface. The barrier for C−O bond cleavage, which results in C adsorbed on Ni(111) and a Mn_4O_4 cluster, is 136 kJ/mol, which is substantially lower than the barrier for CO dissociation on Ni(311). This can explain the higher rate of CO methanation for MnO-promoted Ni (Figure 5). For CO activation, the DFT data show that activation via HCO at the interface site might also be a viable pathway (overall barrier 132 kJ/mol), while the pathway via COH is too difficult (overall barrier 166 kJ/mol). Finally, C and O adsorbed on Ni(111) close to the Mn_4O_4 are hydrogenated to, respectively, CH_4 and H_2O.

Microkinetics simulations predict reaction rates, surface coverages, and the degree of rate control based on the underlying DFT-computed reaction energetics. Figure 10 compares the main simulated kinetic parameters at a temperature of 250 °C for the two models explored in this study. The computed performance data are in good agreement with the experimental results. Specifically, the modeling predicts a substantially higher activity for the Mn_4O_4/Ni(111) system. Overall, the computed turnover frequencies (TOFs) are higher than the experimental ones, which can be explained by the fact that the modeled sites only make up a fraction of the surface of the actual nanoparticles. The apparent activation energy (E_a^{app}) for the more active bimetallic model is also higher than for the Ni(311) model, in line with the experimental results. We can explain these differences by analyzing the composition of the surface adsorbed layer and identifying the rate-controlling elementary reaction steps. Both surfaces display a very high selectivity to CH_4, with a slighlty higher CO selectivity for the Mn_4O_4/Ni(111) model.

For the Ni(311) model, we found that CO_2 adsorption is the step that contributes most to the overall rate control (consistent with the competition between CO_2 desorption and CO_2 activation), followed by direct CO_2 dissociation and C−O bond dissociation by the COH intermediate. The low E_a^{app} derives from the relatively small contributions of the activation energies of the bond breaking steps at the surface. The relatively low reaction rate (despite a low E_a^{app}) is due to a small pre-exponential factor, which can be explained by the substantial loss of entropy in the CO_2 adsorption step. The surface adsorbed layer is mostly composed of H atoms and CO molecules and a small amount of free sites. A reaction path analysis (Figure 10, top panel) shows that adsorbed CO_2 is dissociated in a direct manner to adsorbed CO and O at step-edge sites. COH is the main reaction intermediate undergoing C−O bond cleavage, yielding adsorbed C and OH. The OH is further hydrogenated to H_2O, similar to the O atom origanating from CO_2 dissociation. The C atom is hydrogenated in four facile steps to CH_4. As can be expected for Ni, these carbon hydrogenation steps do not limit the overall reaction rate.

The CO_2 conversion pathways for the Mn_4O_4/Ni(111) model are more complicated. We start the cycle on the defective Mn_4O_3/Ni(111) surface, which contains one O surface vacancy. CO_2 adsorbs strongly on this interface with one of its O atoms located in the O vacancy of the Mn_4O_3 cluster. Cleavage of the activated C−O bond results in CO adsorbed on Ni(111) and reformation of Mn_4O_4. In our modeling, we took into account that one of the O atoms of the Mn_4O_4 cluster can be hydrogenated by H atoms adsorbed at the adjacent terrace surface. The formation of adsorbed H_2O at

DOI: 10.1021/acscatal.9b01968
ACS Catal. 2019, 9, 7823−7839

the cluster and its desorption are steps that partially limit the overall rate.

After removal of one of the O atoms, CO can migrate from the terrace to this cluster on which it can be hydrogenated to a HCO intermediate. This surface species is the main intermediate undergoing C−O bond cleavage at the interface between the Mn-oxide cluster and Ni(111) surface, resulting in a CH intermediate on Ni(111) and the regenerated Mn_4O_4 cluster. The CH intermediate is further hydrogenated on the Ni(111) surface to CH_4, with the last step contributing slightly to the overall degree of rate control (Supporting Information, Figure S22). After hydrogenation of O in Mn_4O_4 to H_2O followed by desorption, the initial Mn_4O_3/Ni(111) surface is regenerated, closing the catalytic cycle.

Besides H_2O formation on the cluster and H_2O desorption, also HCO cleavage at the interface and CO_2 adsorption are rate-controlling steps. In contrast to the Ni(311) surface, the strong adsorption energy of CO_2 on the reduced Mn_4O_3/Ni(111) cluster results in a much lower contribution of adsorption to the degree of rate control (Supporting Information, Figure S22). As the overall reaction is then mainly limited by surface reactions for which entropic changes are much smaller than for adsorption, the predicted activity can be higher than for the Ni(311) in combination with a slightly higher E_a^{app}. The surface adsorbed layer of the bimetallic model can be divided in two components. Similar to the predictions for Ni(311), the Ni(111) surface contains predominantly H atoms and some CO molecules. The CO coverage is higher than on the Ni(311) surface because the overall barrier for CO formation is lower for the Mn_4O_4/Ni(111) model. On the Mn-oxide part, the surface contains predominantly adsorbed O, reflecting the cluster in its oxidized state (without an O vacancy), or with an adsorbed CO molecule. These states are consistent with HCO dissociation and O removal steps being the main rate-controlling steps. Notably, the surface also contains a small amount of bicarbonate (HCO_3^-) and bidentate-bound CO_3^{2-} (bd-CO_3) species formed by reaction of CO_2 with the Mn_4O_4 cluster. This agrees with the experimental IR data. Formate species ($HCOO^-$) are also present in very small quantities, which is in keeping with Figure 9. Microkinetics simulations at temperatures below 200 °C also show that the surface contains a small amount of formate in line with our spectroscopic investigations. The reaction path analysis shows that neither formate nor carbonate/bicarbonate species are involved in C−O bond dissociation reactions. In keeping with our interpretation of the SSITKA data, these species can be regarded as a reservoir of species with a low reactivity. The small amount of CO product is due to desorption of CO from the Ni(111) surface, to which CO binds weaker than to the Ni(111) surface.

3.5. Reactor Modeling. In order to understand the potential of the improved NiMn catalyst, we modeled a Sabatier reactor, which was operated under conditions relevant to a future PtG energy storage concept. As the Sabatier reaction is exothermic, the equilibrium shifts to the reactants with increasing temperature. A proper reactor design including efficient thermal management is required to achieve high CH_4 yields. The optimal Sabatier reactor should approximate a specific temperature profile, matching thermodynamic and kinetic limitations. A metallic Ni catalyst is not active enough to achieve high conversion in the Sabatier reaction.[101] A significantly more active (and expensive) Ru/Al_2O_3 catalyst allowed operating a Sabatier reactor in a successful manner. We base the engineering kinetics for the Ni/TiO_2 and $NiMn/TiO_2$ samples on the simplified kinetic network proposed by Xu and Froment.[85] In this analysis, we did not include the formation of CO, which is a good approximation because the CO yield in our experiments is very low under typical reactor outlet conditions. We first fitted this kinetic model with the activity data available for the Ni/TiO_2 and the optimum $NiMn(1:2)/TiO_2$ catalyst (Supporting Information, Figure S23).

The simulated reactor operates at 10 bar and a space velocity of 3000 h^{-1} and is cooled with an isothermal cooling stream of 200 °C. The most important parameter for the operation of the Sabatier reactor is the reactor activation temperature. This temperature is defined as the minimal feed temperature required to operate the reactor to achieve a sufficiently high CO_2 conversion. This temperature depends on various parameters, including the catalyst used, the pressure and the space velocity.[49] A second important parameter is the maximum conversion attainable within a reasonable residence time in the reactor. This parameter defines the overall performance of the reactor and, for the Sabatier reaction, mainly depends on the low temperature activity of the catalyst. Figure 11 shows the trajectory of the CH_4 yield as a function of the local reactor temperature for the two Ni catalysts and a Ru/Al_2O_3 reference catalyst used in an earlier simulation study.[49] Temperature and concentration profiles along the axial coordinate are given in the Supporting Information (Figure S24). The first main difference is the much higher activation temperature of Ni/TiO_2 compared to Ru/Al_2O_3. The activation temperature around 325 °C for Ni/TiO_2 is in good agreement with the activation temperature for an industrial $Ni/MgAl_2O_4$ catalyst.[82] This has an important effect on the operability of the reactor, since the heat integration and the autothermal operation of the reactor is challenged by the need of preheating the reactants above 300 °C. Interestingly, the difference in activation temperature between the Ru/Al_2O_3 catalyst and the optimum $NiMn/TiO_2$ catalyst is limited: the NiMn catalyst is already active enough to activate the reactor at 240 °C, only 30 °C higher than the reference Ru catalyst. This is an evident advantage compared to the Ni-only catalyst, because it allows autothermal operation of the reactor with a relative facile reactor design.

When the reaction is activated, the reaction rates differ for the three catalysts, which results in different slopes of the lines that describe the initial performance of the reactor. This stage is essentially adiabatic for Ru/Al_2O_3 and $NiMn/TiO_2$ and more affected by cooling for Ni/TiO_2. The nearly straight lines for the two most active catalysts are generated by high reaction rates, which cause a fast heat generation, so that the heat removal rate is not sufficient to avoid the adiabatic operation. The reaction rate on Ni/TiO_2 is lower, so that the cooling system can remove heat from the reactor already in this first stage. When the reactor trajectory reaches the thermodynamic equilibrium, the cooling rate becomes determinant, because the reaction rate is limited by thermodynamics. In this regime, the three catalysts show nearly identical performance and we compute that this area involves about a third of the reactor volume (Figure 11).

When the temperature is reduced, the cooling rate decreases and the reaction becomes kinetically controlled. In this region, the main differences between the three systems are revealed. While Ru/Al_2O_3 and $NiMn/TiO_2$ are active until low temperature, allowing reaching high conversion values, the

DOI: 10.1021/acscatal.9b01968
ACS Catal. 2019, 9, 7823−7839

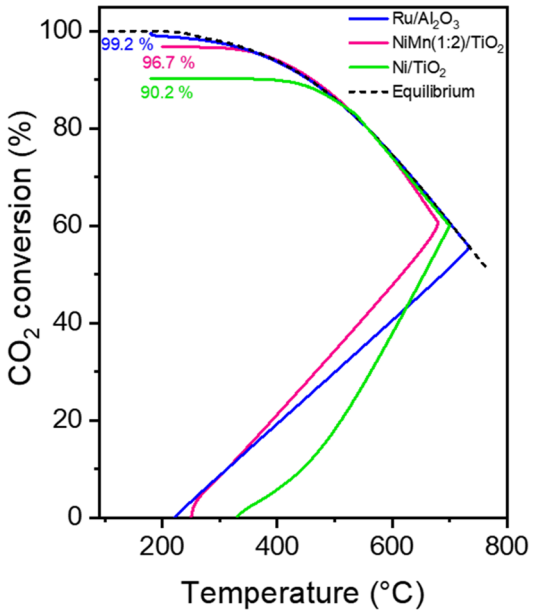

Figure 11. Trajectory in the temperature−CO_2 conversion space of a reference reactor working with Ru/Al_2O_3 (blue line), $NiMn/TiO_2$ (pink line) and Ni/TiO_2 (green line). Note the difference in reaction activation and CO_2 conversion at the reactor outlet.

activity of Ni/TiO_2 is limited to ∼90% conversion within a reasonable residence time. The origin of this has to be traced back to the interplay of kinetics and thermodynamics: above 300 °C high conversion is not attainable because of thermodynamic limitations; below this temperature the catalyst must be active to provide a sufficiently high reaction rate. Ni/TiO_2 is not active enough below 300 °C, so that the outlet conversion remains low. Comparing the two most active systems, we find that the $NiMn/TiO_2$ catalyst can reach a CO_2 conversion of ca. 96%, significantly higher than the Ni/TiO_2 catalyst.

The significance of this analysis of the potential of the $NiMn/TiO_2$ system is in the preliminary design of a reactor with a comparable performance as a standard Ru catalyst. The main advantages of the $NiMn/TiO_2$ catalyst are low temperature activation, good control of hotspots along the reactor coordinate, high activity comparable to Ru above 300 °C, and achievement of a high CO_2 conversion at the cool end of the reactor. In the PtG concept, a conversion above 99% should be targeted. This can be achieved in the same reactor by adding a small finishing bed with Ru/Al_2O_3 catalyst, with the evident benefit in terms of cost compared to the use of Ru/Al_2O_3 in the entire reactor. Notably, the Ni-only catalyst does not have the intrinsic activity to be operated in the same manner, because the additional Ru/Al_2O_3 bed would require a too large volume.

4. CONCLUSIONS

We investigated the influence of Mn loading on Ni/TiO_2 catalysts in CO_2 methanation. Our results show that the addition of Mn to Ni/TiO_2 catalysts leads to significantly enhanced CO_2 methanation activity. This is evident in the reaction activation anticipated of ca. 50 °C compared to a standard Ni catalyst. The promoted catalysts were more stable under CO methanation conditions and considerably less susceptible to deactivation via carbon deposition as shown by TPH. The improved activity originates from the decoration of Ni nanoparticles by highly dispersed MnO, with higher Mn loadings yielding more active methanation catalysts. The overall higher rate of CO_2 methanation for NiMn catalysts related to more facile CO_2 activation, facilitated by the oxophilic nature of defect sites on MnO as shown by FTIR, SSITKA, and DFT. SSITKA measurements confirmed that these formates participate as a CO_2 reservoir, rather than an intermediate in a parallel pathway. The increase in low temperature activity is an important advantage for the design of a Sabatier reactor, allowing reaching conversion above 95% in a single pass reaction and increasing energy efficiency of the PtG system. These findings demonstrate that Ni-based catalysts may be promoted with cheaper and more abundant transition metal oxides such as MnO which can lead to their eventual development and employment on a sustainable and industrial scale.

■ ASSOCIATED CONTENT

Supporting Information

The Supporting Information is available free of charge on the ACS Publications website at DOI: 10.1021/acscatal.9b01968.

Additional catalyst characterization and kinetic data, detailed MKM methods, theoretical modeling, and reactor modeling data (PDF)

■ AUTHOR INFORMATION

Corresponding Author

*Email: e.j.m.hensen@tue.nl.

ORCID

Wilbert L. Vrijburg: 0000-0003-0938-8390
Bart Zijlstra: 0000-0002-4040-6545
Evgeny A. Pidko: 0000-0001-9242-9901
Emiel J. M. Hensen: 0000-0002-9754-2417

Present Addresses

#E.A.P.: Inorganic Systems Engineering group, Department of Chemical Engineering, Delft University of Technology, Van der Maasweg 9, 2629 HZ, Delft, The Netherlands.
‖B.J.P.T.: Inorganic Chemistry and Catalysis, Debye Institute for Nanomaterial Science, Utrecht University, Universiteitsweg 99, 3584 CG Utrecht, The Netherlands.

Notes

The authors declare no competing financial interest.

■ ACKNOWLEDGMENTS

The authors acknowledge financial support from The Netherlands Organization for Scientific Research (NWO) and BASF for a TA-CHIPP grant. Gabriella Garbarino (UNIGE) and Esther Groeneveld (BASF) are thanked for fruitful discussions and guidance. Frans Tichelaar (TU Delft) helped performing the HAADF-STEM EDX measurements. The authors thank Kevin Hermans (TU Eindhoven) for rendering the DFT images. We acknowledge Diamond Light Source for time on beamline B18 under proposal SP16250-1. Tiny Verhoeven, Giulia Spezzati, and Miao Yu (TU Eindhoven) are acknowledged for assistance during XAS measurements, and Adelheid Elemans-Mehring (TU Eindhoven), for performing elemental analysis. The research leading to this result has been supported by the project CALIPSOplus under Grant Agreement 730872 from the EU Framework Programme for Research and Innovation HORIZON 2020.

DOI: 10.1021/acscatal.9b01968
ACS Catal. 2019, 9, 7823−7839

REFERENCES

(1) Gür, T. M. Review of Electrical Energy Storage Technologies, Materials and Systems: Challenges and Prospects for Large-Scale Grid Storage. *Energy Environ. Sci.* **2018**, *11*, 2696−2767.

(2) Sepulveda, N. A.; Jenkins, J. D.; de Sisternes, F. J.; Lester, R. K. The Role of Firm Low-Carbon Electricity Resources in Deep Decarbonization of Power Generation. *Joule* **2018**, *2*, 2403−2420.

(3) Centi, G.; Quadrelli, E. A.; Perathoner, S. Catalysis for CO_2 Conversion: A Key Technology for Rapid Introduction of Renewable Energy in the Value Chain of Chemical Industries. *Energy Environ. Sci.* **2013**, *6*, 1711−1731.

(4) Jentsch, M.; Trost, T.; Sterner, M. Optimal Use of Power-to-Gas Energy Storage Systems in an 85% Renewable Energy Scenario. *Energy Procedia* **2014**, *46*, 254−261.

(5) Götz, M.; Lefebvre, J.; Mörs, F.; McDaniel Koch, A.; Graf, F.; Bajohr, S.; Reimert, R.; Kolb, T. Renewable Power-to-Gas: A Technological and Economic Review. *Renewable Energy* **2016**, *85*, 1371−1390.

(6) Sabatier, P.; Senderens, J. B. *Comptes Rendus Des Séances De L'Académie Des Sciences, Section VI−Chimie*; Imprimerie Gauthier-Villars: Paris, 1902.

(7) Aresta, M.; Dibenedetto, A.; Angelini, A. Catalysis for the Valorization of Exhaust Carbon: From CO_2 to Chemicals, Materials, and Fuels. Technological Use of CO_2. *Chem. Rev.* **2014**, *114*, 1709−1742.

(8) Porosoff, M. D.; Yan, B.; Chen, J. G. Catalytic Reduction of CO_2 by H_2 for Synthesis of CO, Methanol and Hydrocarbons: Challenges and Opportunities. *Energy Environ. Sci.* **2016**, *9*, 62−73.

(9) Otto, A.; Grube, T.; Schiebahn, S.; Stolten, D. Closing the Loop: Captured CO_2 as a Feedstock in the Chemical Industry. *Energy Environ. Sci.* **2015**, *8*, 3283−3297.

(10) Wang, W.; Wang, S.; Ma, X.; Gong, J. Recent Advances in Catalytic Hydrogenation of Carbon Dioxide. *Chem. Soc. Rev.* **2011**, *40*, 3703−3727.

(11) Vogt, C.; Monai, M.; Kramer, G. J.; Weckhuysen, B. M. The Renaissance of the Sabatier Reaction and Its Applications on Earth and in Space. *Nat. Catal.* **2019**, *2*, 188−197.

(12) Rönsch, S.; Schneider, J.; Matthischke, S.; Schlüter, M.; Götz, M.; Lefebvre, J.; Prabhakaran, P.; Bajohr, S. Review on Methanation − From Fundamentals to Current Projects. *Fuel* **2016**, *166*, 276−296.

(13) Boll, W.; Hochgesand, G.; Higman, C.; Supp, E.; Kalteier, P.; Müller, W.-D.; Kriebel, M.; Schlichting, H.; Tanz, H. Gas Production, 3. Gas Treating. In *Ullmann's Encyclopedia of Industrial Chemistry; Major Reference Works*; Wiley-VCH Verlag GmbH & Co. KGaA: Weinheim, Germany, 2011.

(14) Aziz, M. A. A.; Jalil, A. A.; Triwahyono, S.; Ahmad, A. CO_2 Methanation over Heterogeneous Catalysts: Recent Progress and Future Prospects. *Green Chem.* **2015**, *17*, 2647−2663.

(15) Daza, Y. A.; Kuhn, J. N. CO_2 Conversion by Reverse Water Gas Shift Catalysis: Comparison of Catalysts, Mechanisms and Their Consequences for CO_2 Conversion to Liquid Fuels. *RSC Adv.* **2016**, *6*, 49675−49691.

(16) Gao, J.; Liu, Q.; Gu, F.; Liu, B.; Zhong, Z.; Su, F. Recent Advances in Methanation Catalysts for the Production of Synthetic Natural Gas. *RSC Adv.* **2015**, *5*, 22759−22776.

(17) Jalama, K. Carbon Dioxide Hydrogenation over Nickel-, Ruthenium-, and Copper-Based Catalysts: Review of Kinetics and Mechanism. *Catal. Rev.: Sci. Eng.* **2017**, *59*, 95−164.

(18) Wei, W.; Jinlong, G. Methanation of Carbon Dioxide: An Overview. *Front. Chem. Sci. Eng.* **2011**, *5*, 2−10.

(19) Solymosi, F.; Erdohelyi, A.; Kocsis, M. Methanation of CO_2 on Supported Ru Catalysts. *J. Chem. Soc., Faraday Trans. 1* **1981**, *77*, 1003−1012.

(20) Weatherbee, G.; Bartholomew, C. H. Hydrogenation of CO_2 on Group VIII Metals IV. Specific Activities and Selectivities of Silica-Supported Co, Fe, and Ru. *J. Catal.* **1984**, *87*, 352−362.

(21) Kwak, J. H.; Kovarik, L.; Szanyi, J. CO_2 Reduction on Supported Ru/Al_2O_3 Catalysts: Cluster Size Dependence of Product Selectivity. *ACS Catal.* **2013**, *3*, 2449−2455.

(22) Garbarino, G.; Bellotti, D.; Finocchio, E.; Magistri, L.; Busca, G. Methanation of Carbon Dioxide on Ru/Al_2O_3: Catalytic Activity and Infrared Study. *Catal. Today* **2016**, *277*, 21−28.

(23) Panagiotopoulou, P.; Kondarides, D. I.; Verykios, X. E. Selective Methanation of CO over Supported Ru Catalysts. *Appl. Catal., B* **2009**, *88*, 470−478.

(24) Solymosi, F.; Erdöhelyi, A.; Bánsági, T. Methanation of CO_2 on Supported Rhodium Catalyst. *J. Catal.* **1981**, *68*, 371−382.

(25) Trovarelli, A.; Deleitenburg, C.; Dolcetti, G.; Lorca, J. L. CO_2 Methanation Under Transient and Steady-State Conditions over Rh/CeO_2 and CeO_2-Promoted Rh/SiO_2: The Role of Surface and Bulk Ceria. *J. Catal.* **1995**, *151*, 111−124.

(26) Boffa, A.; Lin, C.; Bell, A. T.; Somorjai, G. A. Promotion of CO and CO_2 Hydrogenation over Rh by Metal Oxides: The Influence of Oxide Lewis Acidity and Reducibility. *J. Catal.* **1994**, *149*, 149−158.

(27) Park, J.-N.; McFarland, E. W. A Highly Dispersed Pd−Mg/SiO_2 Catalyst Active for Methanation of CO_2. *J. Catal.* **2009**, *266*, 92−97.

(28) Karelovic, A.; Ruiz, P. Improving the Hydrogenation Function of $Pd/\gamma\text{-}Al_2O_3$ Catalyst by $Rh/\gamma\text{-}Al_2O_3$ Addition in CO_2 Methanation at Low Temperature. *ACS Catal.* **2013**, *3*, 2799−2812.

(29) Gao, J.; Wang, Y.; Ping, Y.; Hu, D.; Xu, G.; Gu, F.; Su, F. A Thermodynamic Analysis of Methanation Reactions of Carbon Oxides for the Production of Synthetic Natural Gas. *RSC Adv.* **2012**, *2*, 2358−2368.

(30) De, S.; Zhang, J.; Luque, R.; Yan, N. Ni-Based Bimetallic Heterogeneous Catalysts for Energy and Environmental Applications. *Energy Environ. Sci.* **2016**, *9*, 3314−3347.

(31) B. Kester, K.; Zagli, E.; L. Falconer, J. Methanation of Carbon Monoxide and Carbon Dioxide on Ni/Al_2O_3 Catalysts: Effects of Nickel Loading. *Appl. Catal.* **1986**, *22*, 311−319.

(32) Garbarino, G.; Riani, P.; Magistri, L.; Busca, G. A Study of the Methanation of Carbon Dioxide on Ni/Al_2O_3 Catalysts at Atmospheric Pressure. *Int. J. Hydrogen Energy* **2014**, *39*, 11557−11565.

(33) Garbarino, G.; Bellotti, D.; Riani, P.; Magistri, L.; Busca, G. Methanation of Carbon Dioxide on Ru/Al_2O_3 and Ni/Al_2O_3 Catalysts at Atmospheric Pressure: Catalysts Activation, Behaviour and Stability. *Int. J. Hydrogen Energy* **2015**, *40*, 9171−9182.

(34) Weatherbee, G. Hydrogenation of CO_2 on Group VIII Metals I. Specific Activity of Ni/SiO_2. *J. Catal.* **1981**, *68*, 67−76.

(35) Weatherbee, G. Hydrogenation of CO_2 on Group VIII Metals II. Kinetics and Mechanism of CO_2 Hydrogenation on Nickel. *J. Catal.* **1982**, *77*, 460−472.

(36) Vogt, C.; Groeneveld, E.; Kamsma, G.; Nachtegaal, M.; Lu, L.; Kiely, C. J.; Berben, P. H.; Meirer, F.; Weckhuysen, B. M. Unravelling Structure Sensitivity in CO_2 Hydrogenation over Nickel. *Nat. Catal.* **2018**, *1*, 127−134.

(37) Zhou, R.; Rui, N.; Fan, Z.; Liu, C. Effect of the Structure of Ni/TiO_2 Catalyst on CO_2 Methanation. *Int. J. Hydrogen Energy* **2016**, *41*, 22017−22025.

(38) Vance, C. K.; Bartholomew, C. H. Hydrogenation of Carbon Dioxide on Group Viii Metals: III, Effects of Support on Activity/Selectivity and Adsorption Properties of Nickel. *Appl. Catal.* **1983**, *7*, 169−177.

(39) Miao, B.; Ma, S. S. K.; Wang, X.; Su, H.; Chan, S. H. Catalysis Mechanisms of CO_2 and CO Methanation. *Catal. Sci. Technol.* **2016**, *6*, 4048−4058.

(40) Karelovic, A.; Ruiz, P. Mechanistic Study of Low Temperature CO_2 Methanation over Rh/TiO_2 Catalysts. *J. Catal.* **2013**, *301*, 141−153.

(41) Muroyama, H.; Tsuda, Y.; Asakoshi, T.; Masitah, H.; Okanishi, T.; Matsui, T.; Eguchi, K. Carbon Dioxide Methanation over Ni Catalysts Supported on Various Metal Oxides. *J. Catal.* **2016**, *343*, 178−184.

(42) Marwood, M.; Doepper, R.; Renken, A. In-Situ Surface and Gas Phase Analysis for Kinetic Studies under Transient Conditions The Catalytic Hydrogenation of CO_2. *Appl. Catal., A* **1997**, *151*, 223−246.

DOI: 10.1021/acscatal.9b01968
ACS Catal. 2019, 9, 7823−7839

(43) Aziz, M. A. A.; Jalil, A. A.; Triwahyono, S.; Mukti, R. R.; Taufiq-Yap, Y. H.; Sazegar, M. R. Highly Active Ni-Promoted Mesostructured Silica Nanoparticles for CO_2 Methanation. *Appl. Catal., B* **2014**, *147*, 359−368.
(44) Wang, X.; Hong, Y.; Shi, H.; Szanyi, J. Kinetic Modeling and Transient DRIFTS−MS Studies of CO_2 Methanation over Ru/Al_2O_3 Catalysts. *J. Catal.* **2016**, *343*, 185−195.
(45) Wu, H. C.; Chang, Y. C.; Wu, J. H.; Lin, J. H.; Lin, I. K.; Chen, C. S. Methanation of CO_2 and Reverse Water Gas Shift Reactions on Ni/SiO_2 Catalysts: The Influence of Particle Size on Selectivity and Reaction Pathway. *Catal. Sci. Technol.* **2015**, *5*, 4154−4163.
(46) Aldana, P. A. U.; Ocampo, F.; Kobl, K.; Louis, B.; Thibault-Starzyk, F.; Daturi, M.; Bazin, P.; Thomas, S.; Roger, A. C. Catalytic CO_2 Valorization into CH_4 on Ni-Based Ceria-Zirconia. Reaction Mechanism by Operando IR Spectroscopy. *Catal. Today* **2013**, *215*, 201−207.
(47) Solis-Garcia, A.; Louvier-Hernandez, J. F.; Almendarez-Camarillo, A.; Fierro-Gonzalez, J. C. Participation of Surface Bicarbonate, Formate and Methoxy Species in the Carbon Dioxide Methanation Catalyzed by ZrO_2-Supported Ni. *Appl. Catal., B* **2017**, *218*, 611−620.
(48) Tada, S.; Kikuchi, R. Mechanistic Study and Catalyst Development for Selective Carbon Monoxide Methanation. *Catal. Sci. Technol.* **2015**, *5*, 3061−3070.
(49) Moioli, E.; Gallandat, N.; Züttel, A. Parametric Sensitivity in the Sabatier Reaction over Ru/Al_2O_3 − Theoretical Determination of the Minimal Requirements for Reactor Activation. *React. Chem. Eng.* **2019**, *4*, 100−111.
(50) Ren, J.; Qin, X.; Yang, J.-Z.; Qin, Z.-F.; Guo, H.-L.; Lin, J.-Y.; Li, Z. Methanation of Carbon Dioxide over Ni−M/ZrO_2 (M = Fe, Co, Cu) Catalysts: Effect of Addition of a Second Metal. *Fuel Process. Technol.* **2015**, *137*, 204−211.
(51) Winter, L. R.; Gomez, E.; Yan, B.; Yao, S.; Chen, J. G. Tuning Ni-Catalyzed CO_2 Hydrogenation Selectivity via Ni-Ceria Support Interactions and Ni-Fe Bimetallic Formation. *Appl. Catal., B* **2018**, *224*, 442−450.
(52) Enger, B. C.; Holmen, A. Nickel and Fischer−Tropsch Synthesis. *Catal. Rev.: Sci. Eng.* **2012**, *54*, 437−488.
(53) Khodakov, A. Y.; Chu, W.; Fongarland, P. Advances in the Development of Novel Cobalt Fischer−Tropsch Catalysts for Synthesis of Long-Chain Hydrocarbons and Clean Fuels. *Chem. Rev.* **2007**, *107*, 1692−1744.
(54) Morales, F.; de Groot, F. M. F.; Gijzeman, O. L. J.; Mens, A.; Stephan, O.; Weckhuysen, B. M. Mn Promotion Effects in Co/TiO_2 Fischer−Tropsch Catalysts as Investigated by XPS and STEM-EELS. *J. Catal.* **2005**, *230*, 301−308.
(55) Morales, F.; de Groot, F. M. F.; Glatzel, P.; Kleimenov, E.; Bluhm, H.; Hävecker, M.; Knop-Gericke, A.; Weckhuysen, B. M. In Situ X-Ray Absorption of Co/Mn/TiO_2 Catalysts for Fischer−Tropsch Synthesis. *J. Phys. Chem. B* **2004**, *108*, 16201−16207.
(56) Bezemer, G. L.; Radstake, P. B.; Falke, U.; Oosterbeek, H.; Kuipers, H. P. C. E.; van Dillen, A. J.; de Jong, K. P. Investigation of Promoter Effects of Manganese Oxide on Carbon Nanofiber-Supported Cobalt Catalysts for Fischer−Tropsch Synthesis. *J. Catal.* **2006**, *237*, 152−161.
(57) Zhao, A.; Ying, W.; Zhang, H.; Hongfang, M.; Fang, D. Ni/Al_2O_3 Catalysts for Syngas Methanation: Effect of Mn Promoter. *J. Nat. Gas Chem.* **2012**, *21*, 170−177.
(58) Wan Abu Bakar, W. A.; Ali, R.; Mohammad, N. S. The Effect of Noble Metals on Catalytic Methanation Reaction over Supported Mn/Ni Oxide Based Catalysts. *Arabian J. Chem.* **2015**, *8*, 632−643.
(59) Zhao, K.; Li, Z.; Bian, L. CO_2 Methanation and Co-Methanation of CO and CO_2 over Mn-Promoted Ni/Al_2O_3 Catalysts. *Front. Chem. Sci. Eng.* **2016**, *10*, 273−280.
(60) Shadravan, V.; Kennedy, E.; Stockenhuber, M. An Experimental Investigation on the Effects of Adding a Transition Metal to Ni/Al_2O_3 for Catalytic Hydrogenation of CO and CO_2 in Presence of Light Alkanes and Alkenes. *Catal. Today* **2018**, *307*, 277−285.
(61) Burger, T.; Koschany, F.; Thomys, O.; Köhler, K.; Hinrichsen, O. CO_2 Methanation over Fe- and Mn-Promoted Co-Precipitated Ni-Al Catalysts: Synthesis, Characterization and Catalysis Study. *Appl. Catal., A* **2018**, *558*, 44−54.
(62) van Haandel, L.; Hensen, E. J. M.; Weber, T. High Pressure Flow Reactor for in Situ X-Ray Absorption Spectroscopy of Catalysts in Gas-Liquid Mixtures—A Case Study on Gas and Liquid Phase Activation of a Co-Mo/Al_2O_3 Hydrodesulfurization Catalyst. *Catal. Today* **2017**, *292*, 51−57.
(63) Chen, W.; Pestman, R.; Zijlstra, B.; Filot, I. A. W.; Hensen, E. J. M. Mechanism of Cobalt-Catalyzed CO Hydrogenation: 1. Methanation. *ACS Catal.* **2017**, *7*, 8050−8060.
(64) Kresse, G.; Hafner, J. Ab Initio Molecular Dynamics for Liquid Metals. *Phys. Rev. B: Condens. Matter Mater. Phys.* **1993**, *47*, 558−561.
(65) Kresse, G.; Furthmüller, J. Efficient Iterative Schemes for Ab Initio Total-Energy Calculations Using a Plane-Wave Basis Set. *Phys. Rev. B: Condens. Matter Mater. Phys.* **1996**, *54*, 11169−11186.
(66) Kresse, G.; Furthmüller, J. Efficiency of Ab-Initio Total Energy Calculations for Metals and Semiconductors Using a Plane-Wave Basis Set. *Comput. Mater. Sci.* **1996**, *6*, 15−50.
(67) Perdew, J. P.; Burke, K.; Ernzerhof, M. Generalized Gradient Approximation Made Simple. *Phys. Rev. Lett.* **1996**, *77*, 3865−3868.
(68) Blöchl, P. E. Projector Augmented-Wave Method. *Phys. Rev. B: Condens. Matter Mater. Phys.* **1994**, *50*, 17953−17979.
(69) Taylor, A. Latice Parameters of Binary Nickel Cobalt Alloys. *J. Inst. Met.* **1950**, *77*, 585−594.
(70) Monkhorst, H. J.; Pack, J. D. Special Points for Brillouin-Zone Integrations. *Phys. Rev. B* **1976**, *13*, 5188−5192.
(71) Liu, J.-X.; Su, Y.; Filot, I. A. W.; Hensen, E. J. M. A Linear Scaling Relation for CO Oxidation on CeO_2 -Supported Pd. *J. Am. Chem. Soc.* **2018**, *140*, 4580−4587.
(72) Vilhelmsen, L. B.; Hammer, B. A Genetic Algorithm for First Principles Global Structure Optimization of Supported Nano Structures. *J. Chem. Phys.* **2014**, *141*, 044711.
(73) Deaven, D. M.; Ho, K. M. Molecular Geometry Optimization with a Genetic Algorithm. *Phys. Rev. Lett.* **1995**, *75*, 288−291.
(74) Daven, D. M.; Tit, N.; Morris, J. R.; Ho, K. M. Structural Optimization of Lennard-Jones Clusters by a Genetic Algorithm. *Chem. Phys. Lett.* **1996**, *256*, 195−200.
(75) Henkelman, G.; Uberuaga, B. P.; Jónsson, H. A Climbing Image Nudged Elastic Band Method for Finding Saddle Points and Minimum Energy Paths. *J. Chem. Phys.* **2000**, *113*, 9901−9904.
(76) Henkelman, G.; Jónsson, H. Improved Tangent Estimate in the Nudged Elastic Band Method for Finding Minimum Energy Paths and Saddle Points. *J. Chem. Phys.* **2000**, *113*, 9978−9985.
(77) Sun, K.; Zhao, Y.; Su, H.-Y.; Li, W.-X. Force Reversed Method for Locating Transition States. *Theor. Chem. Acc.* **2012**, *131*, 1118.
(78) Filot, I. A. W.; Zijlstra, B.; Hensen, E. J. M. *MKMCXX, a C++ Program for Constructing Microkinetic Models*; 2018.
(79) Filot, I. A. W.; van Santen, R. A.; Hensen, E. J. M. The Optimally Performing Fischer−Tropsch Catalyst. *Angew. Chem., Int. Ed.* **2014**, *53*, 12746−12750.
(80) Filot, I. A. W.; Broos, R. J. P.; van Rijn, J. P. M.; van Heugten, G. J. H. A.; van Santen, R. A.; Hensen, E. J. M. First-Principles-Based Microkinetics Simulations of Synthesis Gas Conversion on a Stepped Rhodium Surface. *ACS Catal.* **2015**, *5*, 5453−5467.
(81) Filot, I. A. W.; Zijlstra, B.; Broos, R. J. P.; Chen, W.; Pestman, R.; Hensen, E. J. M. Kinetic Aspects of Chain Growth in Fischer−Tropsch Synthesis. *Faraday Discuss.* **2017**, *197*, 153−164.
(82) Schlereth, D.; Hinrichsen, O. A Fixed-Bed Reactor Modeling Study on the Methanation of CO_2. *Chem. Eng. Res. Des.* **2014**, *92*, 702−712.
(83) Sun, D.; Simakov, D. S. A. Thermal Management of a Sabatier Reactor for CO_2 Conversion into CH_4: Simulation-Based Analysis. *J. CO2 Util.* **2017**, *21*, 368−382.
(84) Falbo, L.; Martinelli, M.; Visconti, C. G.; Lietti, L.; Bassano, C.; Deiana, P. Kinetics of CO_2 Methanation on a Ru-Based Catalyst at Process Conditions Relevant for Power-to-Gas Applications. *Appl. Catal., B* **2018**, *225*, 354−363.

DOI: 10.1021/acscatal.9b01968
ACS Catal. 2019, 9, 7823−7839

(85) Xu, J. G.; Froment, G. F. Methane Steam Reforming, Methanation and Water-Gas Shift: I. Intrinsic Kinetics. *AIChE J.* **1989**, *35*, 88−96.
(86) Morales, F.; de Smit, E.; de Groot, F. M. F.; Visser, T.; Weckhuysen, B. M. Effects of Manganese Oxide Promoter on the CO and H_2 Adsorption Properties of Titania-Supported Cobalt Fischer−Tropsch Catalysts. *J. Catal.* **2007**, *246*, 91−99.
(87) Ettireddy, P. R.; Ettireddy, N.; Mamedov, S.; Boolchand, P.; Smirniotis, P. G. Surface Characterization Studies of TiO_2 Supported Manganese Oxide Catalysts for Low Temperature SCR of NO with NH_3. *Appl. Catal., B* **2007**, *76*, 123−134.
(88) Dietz, L.; Piccinin, S.; Maestri, M. Mechanistic Insights into CO_2 Activation via Reverse Water−Gas Shift on Metal Surfaces. *J. Phys. Chem. C* **2015**, *119*, 4959−4966.
(89) Olesen, S. E.; Andersson, K. J.; Damsgaard, C. D.; Chorkendorff, I. Deactivating Carbon Formation on a Ni/Al_2O_3 Catalyst under Methanation Conditions. *J. Phys. Chem. C* **2017**, *121*, 15556−15564.
(90) Seok, S.-H.; Choi, S. H.; Park, E. D.; Han, S. H.; Lee, J. S. Mn-Promoted Ni/Al_2O_3 Catalysts for Stable Carbon Dioxide Reforming of Methane. *J. Catal.* **2002**, *209*, 6−15.
(91) Pan, Q.; Peng, J.; Wang, S.; Wang, S. In Situ FTIR Spectroscopic Study of the CO_2 Methanation Mechanism on $Ni/Ce_{0.5}Zr_{0.5}O_2$. *Catal. Sci. Technol.* **2014**, *4*, 502−509.
(92) Pan, Q.; Peng, J.; Sun, T.; Wang, S.; Wang, S. Insight into the Reaction Route of CO_2 Methanation: Promotion Effect of Medium Basic Sites. *Catal. Commun.* **2014**, *45*, 74−78.
(93) Kantcheva, M.; Kucukkal, M. U.; Suzer, S. Spectroscopic Investigation of Species Arising from CO Chemisorption on Titania-Supported Manganese. *J. Catal.* **2000**, *190*, 144−156.
(94) Agnelli, M.; Swaan, H. M.; Marquez-Alvarez, C.; Martin, G. A.; Mirodatos, C. CO Hydrogenation on a Nickel Catalyst. *J. Catal.* **1998**, *175*, 117−128.
(95) Shannon, S. L.; Goodwin, J. G. Characterization of Catalytic Surfaces by Isotopic-Transient Kinetics during Steady-State Reaction. *Chem. Rev.* **1995**, *95*, 677−695.
(96) van Helden, P.; Ciobîcă, I. M.; Coetzer, R. L. J. The Size-Dependent Site Composition of FCC Cobalt Nanocrystals. *Catal. Today* **2016**, *261*, 48−59.
(97) Bezemer, G. L.; Bitter, J. H.; Kuipers, H. P. C. E.; Oosterbeek, H.; Holewijn, J. E.; Xu, X.; Kapteijn, F.; van Dillen, A. J.; de Jong, K. P. Cobalt Particle Size Effects in the Fischer−Tropsch Reaction Studied with Carbon Nanofiber Supported Catalysts. *J. Am. Chem. Soc.* **2006**, *128*, 3956−3964.
(98) Ren, J.; Guo, H.; Yang, J.; Qin, Z.; Lin, J.; Li, Z. Insights into the Mechanisms of CO_2 Methanation on Ni(111) Surfaces by Density Functional Theory. *Appl. Surf. Sci.* **2015**, *351*, 504−516.
(99) Fan, C.; Zhu, Y.-A.; Yang, M.-L.; Sui, Z.-J.; Zhou, X.-G.; Chen, D. Density Functional Theory-Assisted Microkinetic Analysis of Methane Dry Reforming on Ni Catalyst. *Ind. Eng. Chem. Res.* **2015**, *54*, 5901−5913.
(100) Liu, J.-X.; Su, H.-Y.; Sun, D.-P.; Zhang, B.-Y.; Li, W.-X. Crystallographic Dependence of CO Activation on Cobalt Catalysts: HCP versus FCC. *J. Am. Chem. Soc.* **2013**, *135*, 16284−16287.
(101) Mutschler, R.; Moioli, E.; Luo, W.; Gallandat, N.; Züttel, A. CO_2 Hydrogenation Reaction over Pristine Fe, Co, Ni, Cu and Al_2O_3 Supported Ru: Comparison and Determination of the Activation Energies. *J. Catal.* **2018**, *366*, 139−149.

DOI: 10.1021/acscatal.9b01968
ACS Catal. 2019, 9, 7823−7839